SERI/PR-9272-1-T1

NOVEL CONCEPTS IN ELECTROCHEMICAL SOLAR CELLS

Quarterly Technical Progress Report, December 15, 1980—March 15, 1981

Work Performed Under Contract No. AC02-77CH00178

Research Institute of Colorado
Fort Collins, Colorado

U.S. Department of Energy

Solar Energy

DISCLAIMER

DISCLAIMER

SERI/PR-9272-1-T1
Distribution Category UC-61c

NOVEL CONCEPTS IN ELECTROCHEMICAL SOLAR CELLS

Quarterly Technical Progress Report
For the Period December 15, 1980-March 15, 1981

Research Institute of Colorado
Subcontract No. XS-0-9272-1

under

Prime Contract No. EG-77-C-01-4042
Midwest Research Institute
Solar Energy Research Institute

Krishnan Rajeshwar-Acting Program Manager

THIS PAGE

WAS INTENTIONALLY

LEFT BLANK

ACKNOWLEDGEMENT

We thank R. Thapar, P. Smith, T. Mraz and L. Thompson for carrying out the experiments reported herein.

The CdSe thin-film electrodes were prepared by Professor K.L. Chopra's group at the Indian Institute of Technology, New Delhi.

TABLE OF CONTENTS

1. INTRODUCTION

During the past quarter, the following areas were emphasized (a) Characterization of redox couples with very positive potentials in room-temperature $AlCl_3$-BPC electrolytes and comparison of the electrochemical behavior of decamethyl ferrocene in these electrolytes with the previously-studied ferrocene/ferricenium ion couple, (b) Photoelectrochemical characterization of CdSe thin-film anodes in aqueous polysulfide electrolytes and (c) Refinement of the admittance measurement technique for extraction of Mott-Schottky parameters. The results of our research in these areas are detailed in turn below.

RESULTS AND DISCUSSIONS

2 PHOTOELECTROCHEMICAL OXIDATION OF DECAMETHYL FERROCENE AND AROMATIC HYDROCARBONS AT THE n-GaAs/$AlCl_3$-BPC INTERFACE

Cyclic Voltammetry on Carbons

Decamethyl Ferrocene. Figure 1 shows representative cyclic voltammograms on carbon for $(\eta^5 - (CH_3)_5\ C_5)_2$ Fe in the $AlCl_3$-BPC electrolyte. Relevant data on various parameters extracted from these plots are assembled in Table 1. The cathodic shift in the peak for reduction of the cation with increasing scan rate is consistent with an inherently sluggish charge transfer step [7]. This in turn is reflected in a concomitant increase in the peak separation approaching values which are significantly greater than those predicted by theory ($\Delta V_p \simeq 60$ mV for one-electron charge transfer) at scan rates ≥ 50 mV-s^{-1}. The peak ratios (estimated by the semi-empirical procedure, ref. 8) remain sensibly close to unity although the systematic variation in the ratio, cathodic peak current/$(\text{scan rate})^{1/2}$ suggests that rate control may not be exercised by diffusion of electroactive species alone. The peak potentials for the oxidation reaction, however, shows no dependence on

Figure 1: Cyclic voltammograms on carbon for decamethyl ferrocene. The $AlCl_3$-BPC electrolyte had a mole ratio composition of ~1.2:1.

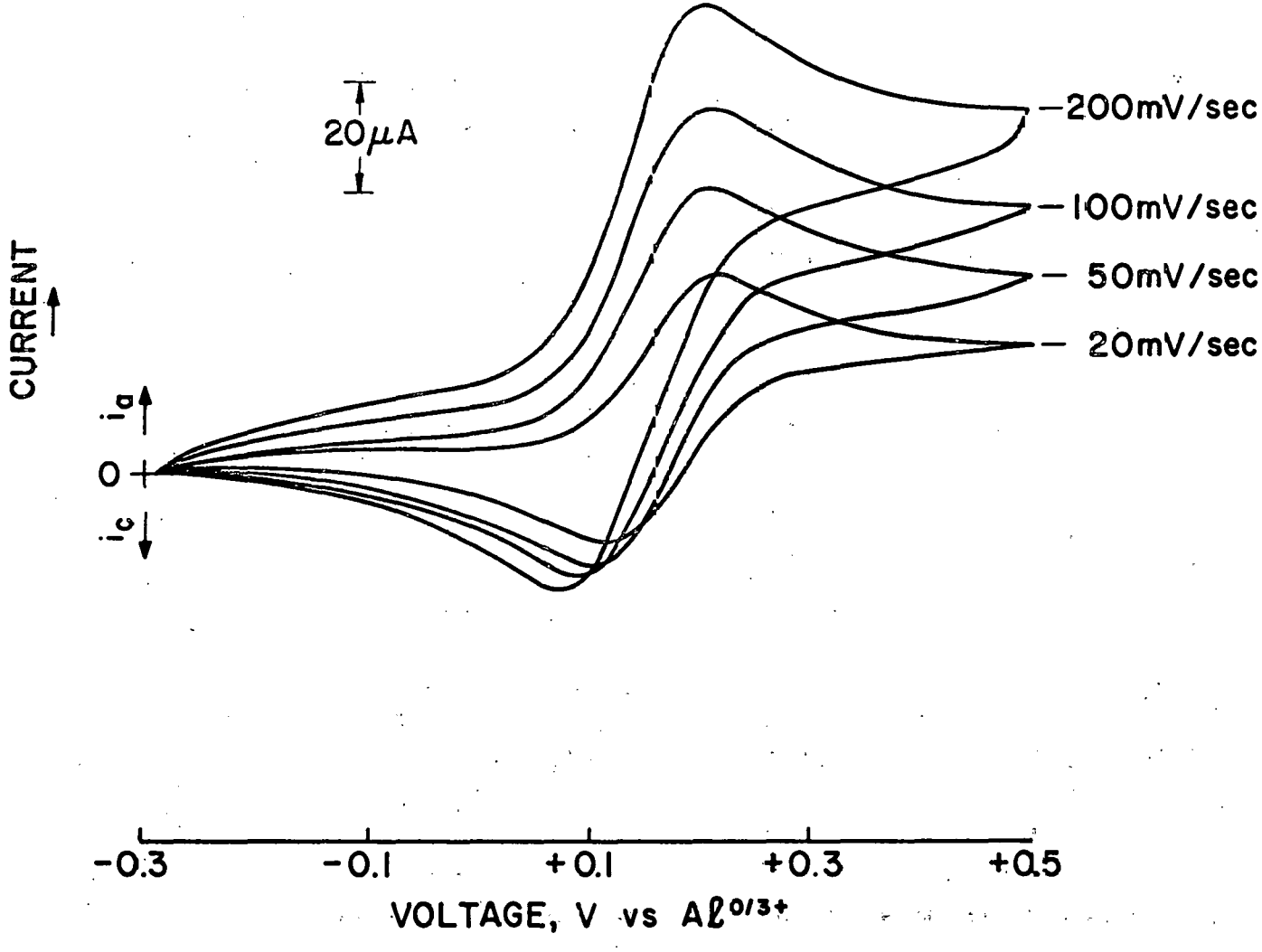

TABLE 1

Cyclic Voltammetry Data on Carbon for Decamethyl Ferrocene and Aromatic Hydrocarbons in the $A\ell C\ell_3$-BPC Electrolyte

Species	Scan Rate mV/sec	V_p^a V vs. $A\ell^{\circ/3+}$	V_p^c V vs. $A\ell^{\circ/3+}$	$\Delta V_p = V_p^a - V_p^c$ V	$V_{1/2} = \frac{(V_p^a + V_p^c)}{2}$ V vs. $A\ell^{\circ/3+}$	i_p^c/i_p^a	$i_p^c/(\text{scan rate})^{1/2}$ $\mu A(\text{sec})^{1/2}\ (\text{mv})^{-12}$
$[\eta^5-(CH_3)_5C_5)_2$ Fe	20	+0.210	+0.115	0.095	+0.16	1.06	3.80
	50	+0.210	+0.105	0.105	+0.16	0.96	3.82
	100	+0.210	+0.100	0.100	+0.16	0.99	3.50
	200	+0.210	+0.085	0.125	+0.15	0.88	3.04
BP	20	+1.24	+1.12	0.12	+1.18	0.55	22.37
	50	+1.27	+1.12	0.15	+1.20	0.75	14.14
	100	+1.275	+1.13	0.145	+1.20	0.87	10.00
	200	+1.30	+1.15	0.15	+1.23	0.92	6.72
DPA	20	+1.48	+1.375	0.105	+1.43	1.09	2.68
	50	+1.49	+1.375	0.115	+1.44	1.09	2.83
	100	+1.50	+1.375	0.125	+1.44	1.05	2.93
	200	+1.50	+1.375	0.125	+1.44	1.00	3.11
A	20	+1.65	+1.475	0.100	+1.57	1.67	6.04
	50	+1.675	+1.475	0.20	+1.58	1.59	6.36
	100	+1.725	+1.475	0.25	+1.61	1.56	7.20
	200	+1.750	+1.475	0.27	+1.62	1.35	9.55
HMB	20	+1.58	--	--	+1.44[a)]	--	--
	50	+1.63	--	--	+1.44	--	--
	100	+1.66	--	--	+1.53	--	--
	200	+1.72	--	--	+1.59	--	--

a) The potentials refer to $V_{p/2}$ values, i.e., the potentials at which the currents are half their peak values.

scan rate indicating relatively facile charge transfer in the anodic direction. The above data on $(\eta^5 - (CH_3)_5\ C_5)_2$ Fe are consistent with "quasi-reversible" behavior with significant asymmetry associated with the charge transfer step.

The data in Figure 1 and Table 1 were obtained for the $A\ell C\ell_3$-BPC electrolyte adjusted to be slightly acidic ($A\ell C\ell_3$-BPC molar ratio = 1.2:1) of the neutral composition. A previous study in the laboratory had shown that the oxidation potential of $(\eta^5 - (CH_3)_5\ C_5)_2$ Fe is dependent on melt acidity [9] (by way of contrast, the redox behavior of ferrocene is independent of melt acidity, refs. 1a., 3). In basic $A\ell C\ell_3$-BPC electrolytes, $V_{p/2}$ (defined here as $(V_p^a + V_p^c)/2$, cf., Table 1) was found to occur at -0.29 V. Moreover, a further oxidation is possible in acidic ($\geq$ 1.5:1) electrolytes ($V_{p/2}$ = +1.38 V) yielding the decamethyl ferricenium dication [9]. No attempt was made in this study to further characterize this oxidation step.

Aromatic Hydrocarbons

Table 1 summarizes the results of cyclic voltammetry on carbon for the aromatic hydrocarbons selected for this study. In all cases, the composition of the $A\ell C\ell_3$-BPC electrolyte was adjusted to be acidic ($\sim$1.5:1). This particular composition was selected for two reasons: (a) the potential limit on the anodic side for basic electrolytes lies cathodic (by $\sim$ 1 V) of that for acid systems and therefore is inaccessible to the potentials required for hydrocarbon oxidation, and (b) a previous study [3] had shown that in more acidic electrolytes, the hydrocarbon is spontaneously oxidized to the cation radical.

The electrochemical behavior for each individual compound in Table 1 is amplified in the following paragraphs.

The anodic shift in V_p^a with increasing scan rate for BP is consistent with a sluggish oxidation reaction. The V_p^c values, on the other hand, are less sensitive to scan rate suggesting asymmetry in the efficacy of charge transfer in the two directions for this compound (cf., the case of $(\eta^5 - (CH_3)_5\ C_5)_2$ Fe, vide supra). The ΔV_p values are much higher than those typical of reversible charge transfer. Moreover, the systematic increase in the peak current ratio with increasing scan rate indicates that the product of the electron transfer is undergoing a following chemical reaction.

Somewhat more ideal behavior is observed for DPA. The relative insensitivity of peak potentials and the peak current ratio to scan rate is consistent with more facile charge transfer and relatively higher stability of the cation radical respectively. The peak separation potentials, however, are still quite high even at the lowest scan rate employed (Table 1). Figure 2 illustrates representative cyclic voltammograms for this material.

Even more drastic departures from ideality (relative to the case of BP) are noted for A (cf., Table 1). The V_p^a values show a pronounced anodic shift with increasing scan rate while the V_p^c values are insensitive (cf., the case of BP and A above). The ΔV_p values show the highest departure from ideal behavior relative to the other systems in the present study. The peak current ratios deviate significantly from unity especially at low scan rates, indicating the relative instability of the $A^{+\cdot}$ radical. Essentially similar behavior was noted by previous authors [3] who additionally observed oxidation to the dication at +1.82 V.

Behavior more extreme than that noted above is typified by the case of HMB which shows irreversible charge transfer at scan rates up to

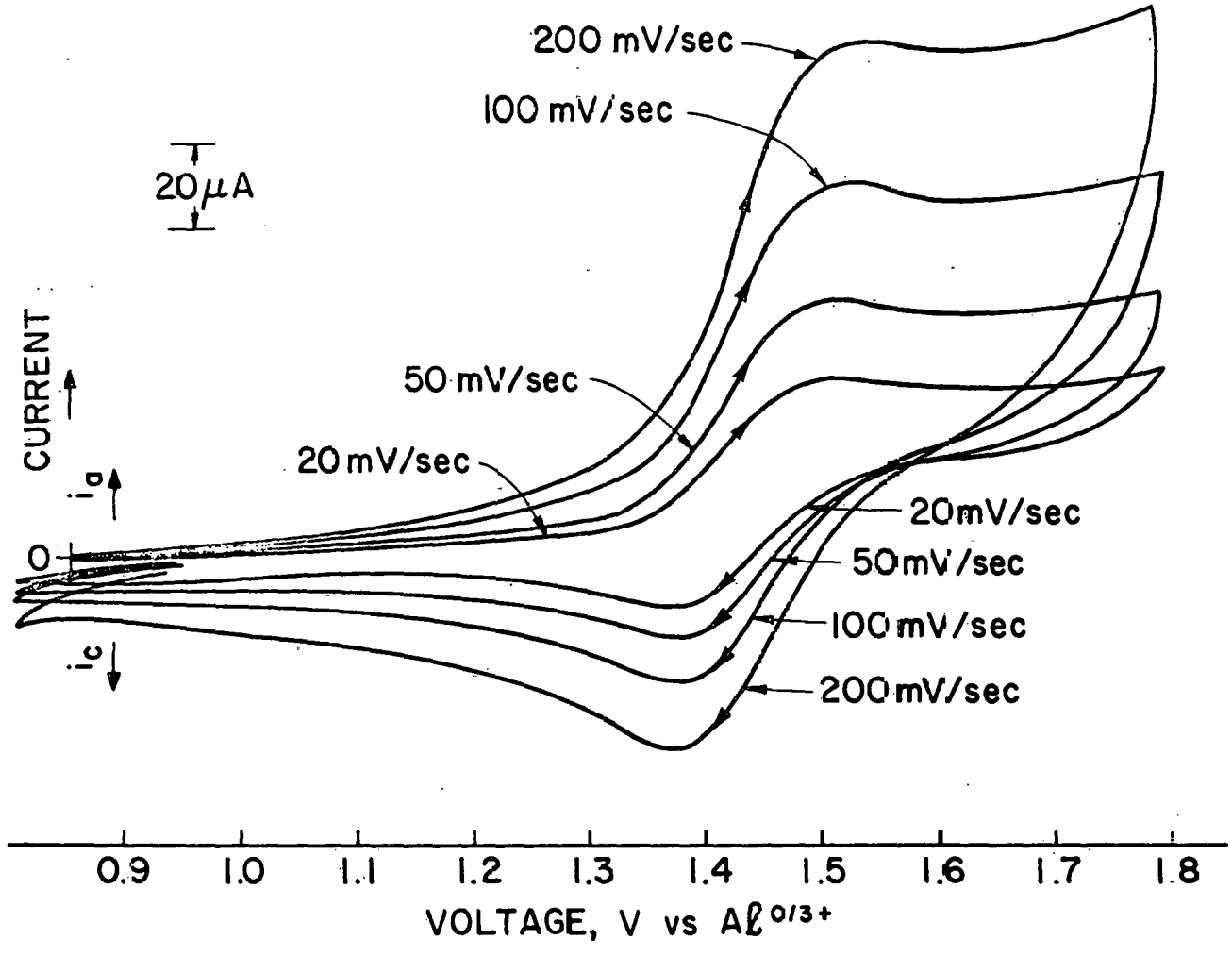

Figure 2: Cyclic voltammograms on carbon for 9, 10 - diphenyl anthacene in $AlCl_3$-BPC electrolyte.

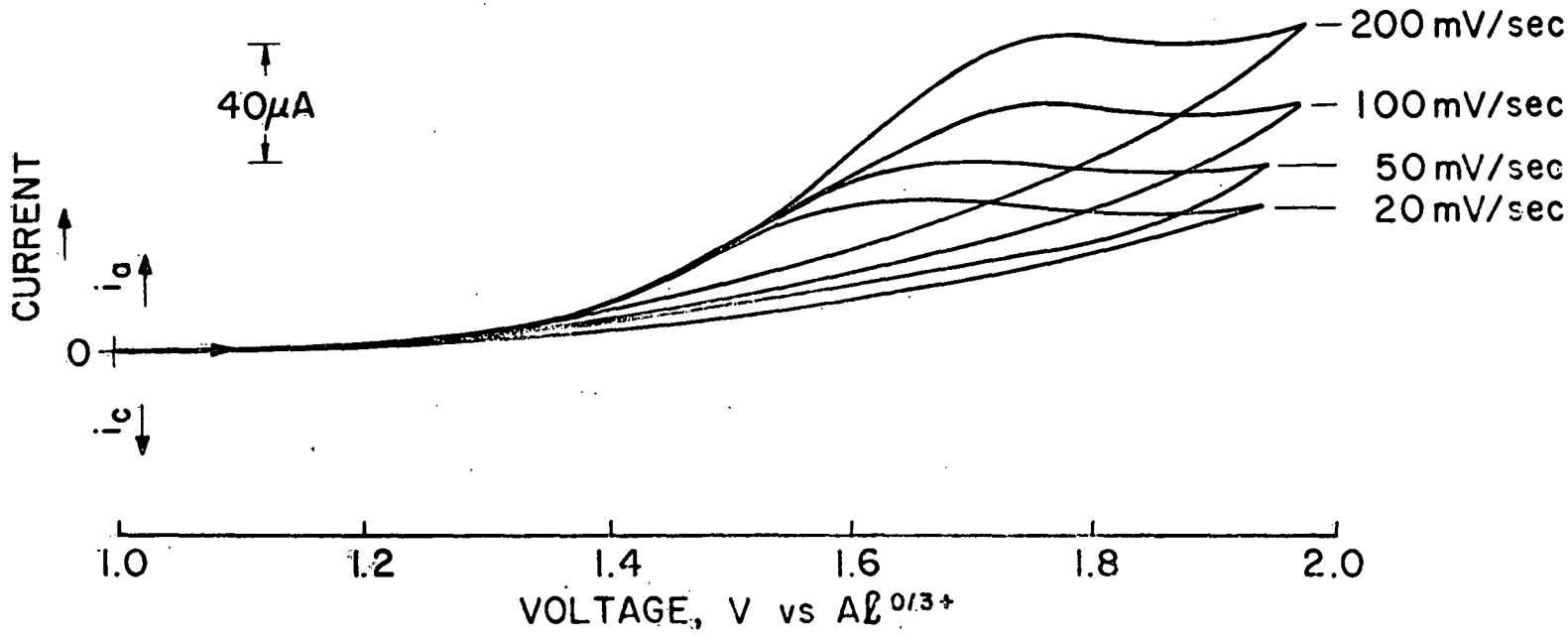

Figure 3: Cyclic voltammograms on carbon for hexamethyl benzene in $AlCl_3$-BPC electrolyte.

200 mV/s (Figure 3). Moreover, the V_p^a values are again dependent on scan rate to a pronounced degree (Table 1) indicating a rather sluggish deeclectronation step. Previous authors have observed a reduction wave for the HMB radical at scan rates above 1 V s^{-1} [3]. Essentially similar behavior (irreversible oxidation at scan rates < 10 Vs^{-1}) has also been observed for this compound in $A\ell C\ell_3$-ethyl pyridinium bromide electrolyte [5].

The $V_{p/2}$ values obtained for BP, DPA, A and HMB in the present study lie slightly positive of values reported by previous authors [3]. These authors also report that their values are independent of the melt composition and scan rate up to 5 Vs^{-1}. While the former conclusion is supported by the results of this study, only in the case of DPA were the peak potentials insensitive to scan rate (cf., Table 1). The other compounds showed intrinsically sluggish electrochemical behavior as shown by the systematic dependence of V_p^a and ΔV_p on scan rate. Based on the results of the present study and the criteria set forth by previous authors [7] for the elucidation of electrode kinetics by cyclic voltammetry, the cation radical stability and the charge transfer kinetics may be ordered thus: DPA >> BP > A > HMB.

Cyclic voltammograms, essentially similar to those obtained for the neat $A\ell C\ell_3$-BPC/electrolytes (cf., Figures 2 and 3) were seen for the $A\ell C\ell_3$-BPC/toluene mixtures (50 v/v solutions). The peak separation potentials were not significantly affected in the presence of toluene confirming that solution conductivity was not playing a major role in the magnitude of the observed ΔV_p values, vide supra. (Previous studies [10] had shown that the admixture of organic solvents with $A\ell C\ell_3$-BPC electrolytes results in a marked enhancement of the viscosity and conductivity of the latter.) The peak potentials were shifted somewhat cathodic of values in neat $A\ell C\ell_3$-BPC systems (Table 3).

Decamethyl Ferrocene

A previous study in this laboratory had established that melt acidity plays a critical role in determining the efficacy of charge transfer at the n-GaAs/$A\ell C\ell_3$-BPC interface containing the ferrocene/ferricenium in redox system [1]. In particular, the possibility of moving the semiconductor band edges up or down relative to the redox level (by appropriate adjustment of the relative mole ratios of $A\ell C\ell_3$ and BPC) offers a convenient means of mapping energy levels (e.g., surface states). A clear illustration of this approach is provided by the results in Figure 4. Figure 4(a) illustrates cyclic voltammograms obtained in the dark and under band-gap illumination of n-GaAs electrodes in contact with $(\eta^5\ (CH_3)_5\ C_5)_2$ Fe species in the $A\ell C\ell_3$-BPC electrolyte. The $A\ell C\ell_3$-BPC electrolyte was adjusted to be acidic ($A\ell C\ell_3$-BPC = 1.2:1). No photoeffect is observed for this particular electrolyte composition. The background reduction currents represent electrolyte decomposition effects discussed in detail elsewhere [1a, 11]. Figure 4(b) shows the data obtained on the same electrode in contact with the above electrolyte to which a small amount of BPC was added. Photooxidation of $(\eta^5$ - $(CH_3)_5\ C_5)_2$ Fe species is now clearly visible with a peak at $\sim$ -0.05 V. The photogenerated species are reduced on the reverse cathodic sweep at $\sim$ -0.15 V. When the light is shut off at the anodic potential limit, the anodic current immediately dies to zero, with a reduction peak still visible at $\sim$ -0.15 V. This peak is greatly attenuated on the second successive cathodic sweep with the oxidation peak completely absent on the anodic cycle. These results confirm the origin of the peaks as being due to the photooxidation and subsequent reduction of the elctroactive $(\eta^5$ - $(CH_3)_5\ C_5)_2$ Fe species. Note that the oxidation occurs at a potential $\sim$200 mV <u>negative</u> of that

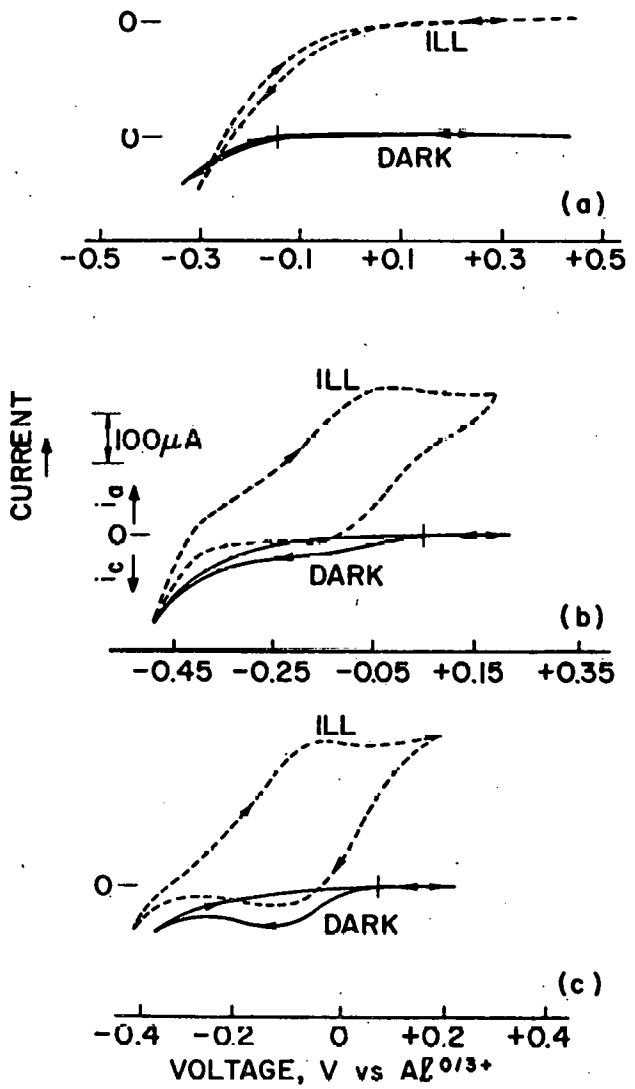

Figure 4: Cyclic voltammograms in the dark and under illumination for n-GaAs electrodes in contact with decamethyl ferrocene on the $A\ell Cl_3$-BPC electrolyte. The data in Figure 4(a) refer to the 1.2:1 electrolyte and those in 4(b) and 4(c) represent increasing additions of BPC to this composition (see text). The illumination intensity (uncorrected) was ~80 mW/cm^2.

on carbon (the equilibrium potential for $(\eta^5 - (CH_3)_5\ C_5)_2$ Fe in this electrolyte is still +0.16 V (Table 1) and has not shifted by addition of BPC as shown by a cyclic voltammetry scan on carbon) underscoring the contribution of light energy to the total energy required for the oxidation reaction.

Figure 4(c) shows the data on addition of further BPC to the above electrolyte (cf., Figure 4(b)). Behavior essentially similar to that in Figure 4(b) is observed with the oxidation peak displaced slightly more negative of the value in Figure 4(b). A reduction peak at -0.1 V which is barely discernible in the data in Figure 4(b) is, however, observed in the dark. This peak may have its origin in the reduction of some electrolyte species. A similar reduction was observed in the case of ferrocene and also for decamethyl ferrocene in very basic electrolytes (vide infra) [12].

The data in Figure 4 may be rationalized as follows. On addition of BPC to the 1.2:1 electrolyte, the semiconductor band-edges are shifted towards negative potentials because of specific ion adsorption [1,13]. The net result is a shift in the relative disposition of the semiconductor energy levels and the redox couple (which remains relatively fixed over the range of electrolyte compositions in Figure 4, vide supra). The onset of photooxidation as seen in Figure 4(b) and the absence of this photoeffect in Figure 4(a) indicate that surface states are introduced in the n-GaAs band gap by specific adsorption of $C\ell^-$ ions. The photooxidation is mediated by these band-gap states which are presumably absent in the case of the electrolyte in Figure 4(a) because of the lack of free (uncomplexed) $C\ell$ species [1]. The reduction of the photogenerated species is also probably mediated by surface states (cf.,

ref. 1a). On the basis of the data in Figure 4, these surface states at the n-GaAs/$A\ell C\ell_3$-BPC interface seem to be located at an energy ~0.6 eV below the conduction band-edge.

In the 0.8:1 electrolyte, photooxidation of $(\eta^5 - (CH_3)_5\ C_5)_2$ Fe on n-GaAs occurs at ~110 mV negative of the oxidation potential on carbon ($V_{p/2}$: =-0.29V) in this system [9,12]. The reduction peak for the photooxidized species occurs at ~ -0.48 V. Therefore, regardless of the electrolyte composition (excluding acidic systems, cf., Figure 4(a)), photooxidation of $(\eta^5 - (CH_3)_5\ C_5)_2$ Fe is sustained on n-GaAs electrodes at potentials well negative of their equilibrium (thermodynamic) values.

No perceptible degradation of the n-GaAs surface occurred (as judged by visual examination) during these photooxidation experiments, indicating that the electrode corrosion reaction was effectively suppressed (cf., the case of ferrocene, ref. 1a).

Aromatic Hydrocarbons

In the dark, the cyclic voltammograms on n-GaAs were featureless for all the hydrocarbons included in the present study. This behavior is readily understood in terms of the simple model for semiconductor/electrolyte interfaces [14] since the redox couples lie well positive of the conduction band edge (~ -0.3 V) in the 1.5:1 electrolyte.

Cyclic voltammetry data on illumination of n-GaAs electrodes are assembled in Table 2 for the various hydrocarbons. Note that in all the cases, the peak potentials corresponding to the photooxidation(s) occur at potentials well negative of corresponding values on carbon (compare Table 1 and 2). In each case, the photoprocesses were confirmed by switching off the light at the anodic potential limit. The currents immediately died down. Typical cyclic voltammograms are shown in Figures 5 and 6 for DPA and A respectively. In the case of HMB, no

TABLE 2

Cyclic Voltammetry data[a] on illuminated n-GaAs electrodes (light intensity: ~100 mW/cm^2) in the $A\ell Cl_3$-BPC electrolyte

Species	V_p^a [b] V vs. $A\ell^{0/3+}$	V_p^c [b] V vs. $A\ell^{0/3+}$
BP	0.95	0.63
DPA	0.88, 1.15	0.85, 1.10
A	1.20,[c] 1.40	0.85, 1.16
HMB	0.70[d]	---

a) Scan Rate: 100 mV/s.

b) Only values recorded on the first sweep are shown.

c) Incompletely resolved, cf., Figure 6.

d) Potential at the foot of the anodic wave.

oxidation waves were observed although a gradual increase in photocurrents was noted over the entire range of the potential scan (0 to +1.9 V). The onset potential was well positive of the flat-band value for this system (Table 2). It is pertinent to note here that photooxidation of HMB is sustained on n-GaAs in spite of the fact that the oxidation potential ($\sim$ +1.7 V, Table 1) lies positive of the valence band edge ($E_{VB}/_q$ = +1.1 V) in this electrolyte. Similar anomalous behavior has been noted by previous authors for n-GaAs electrodes in acetonitrile [15]. These effects may be due to band edge "unpinning" caused by surface states and have been discussed elsewhere [15].

Interesting effects were observed for DPA and A in that their cyclic voltammograms on n-GaAs showed two oxidation and reduction waves (Figures 5 and 6), the former being resolved to varying degrees on the two systems depending on the scan rate employed. These peak positions are listed in Table 2 and may be ascribed to the following sequence of steps:

$$\text{semiconductor} \xrightarrow{h\nu} e^- + h^+ \qquad (1a)$$

$$Ar + h^+ \xrightarrow{h\nu} Ar^{+\cdot} \qquad (1b)$$

$$Ar^{+\cdot} \longrightarrow Ar^{++} + e^- \text{ (conduction band)} \qquad (1c)$$

where Ar, $Ar^{+\cdot}$, Ar^{++} denote the hydrocarbon, cation radical and dication respectively, and e^- and h^+ represent the photogenerated electron-hole pairs. The formation of the dication is facilitated by injection of an electron into the conduction band in n-GaAs. This process is reminiscent of the "current-doubling" mechanism noted previously for radical species on various semiconductors [16]. The absence of this effect for BP in the present study (Table 2) may indicate the importance of factors related to the reorganization energy

Figure 5: Cyclic voltammogram on n-GaAs in $A\ell Cl_3$-BPC electrolyte containing 9, 10 - diphenyl anthracene. Scan rate: 100 mV/sec; light intensity: ~100 mW/cm^2.

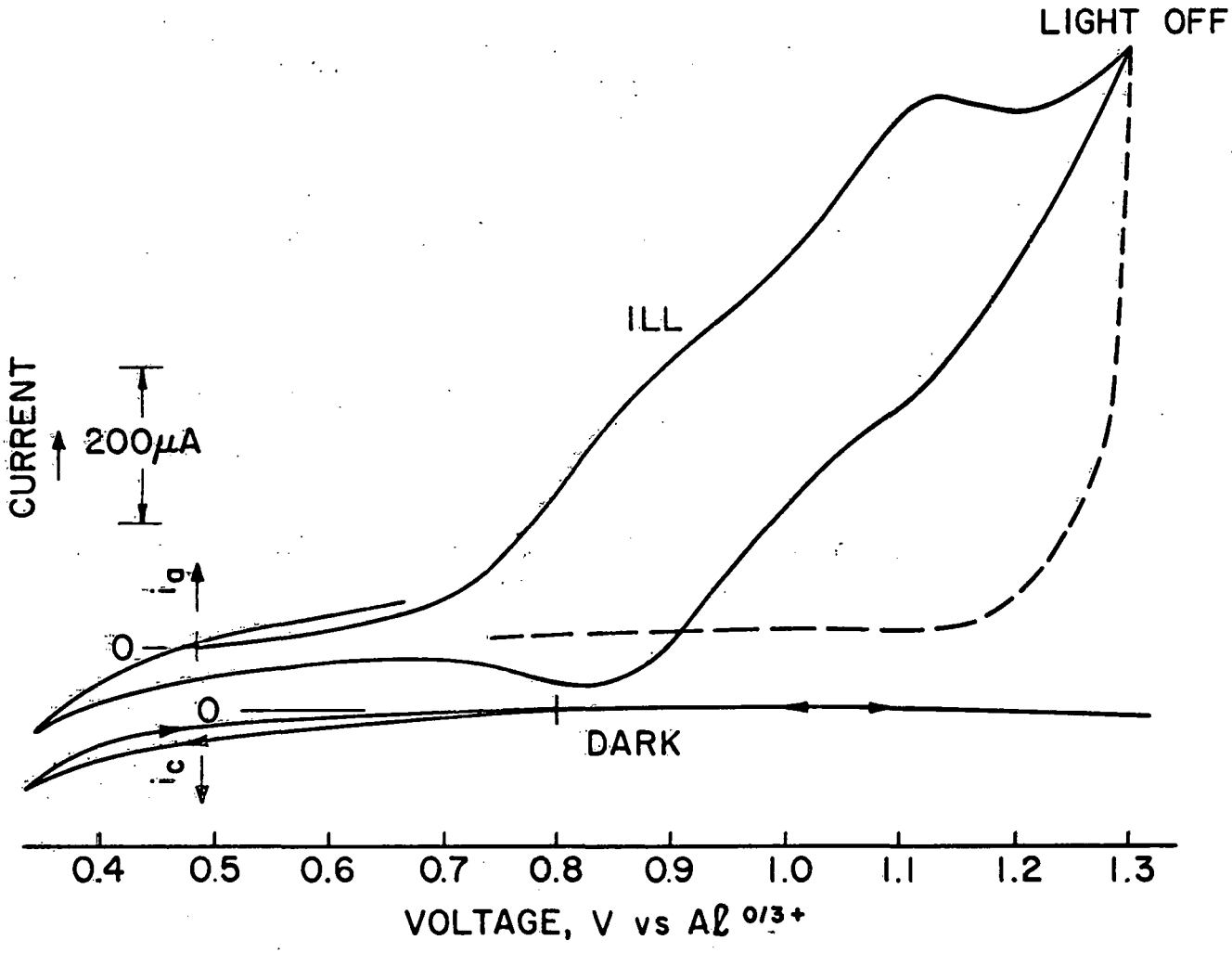

Figure 6: Cyclic voltammograms on n-GaAs in $AlCl_3$-BPC electrolyte containing anthracene. Scan rate: 100 mV/sec; light intensity: ~100 mW/cm^2.

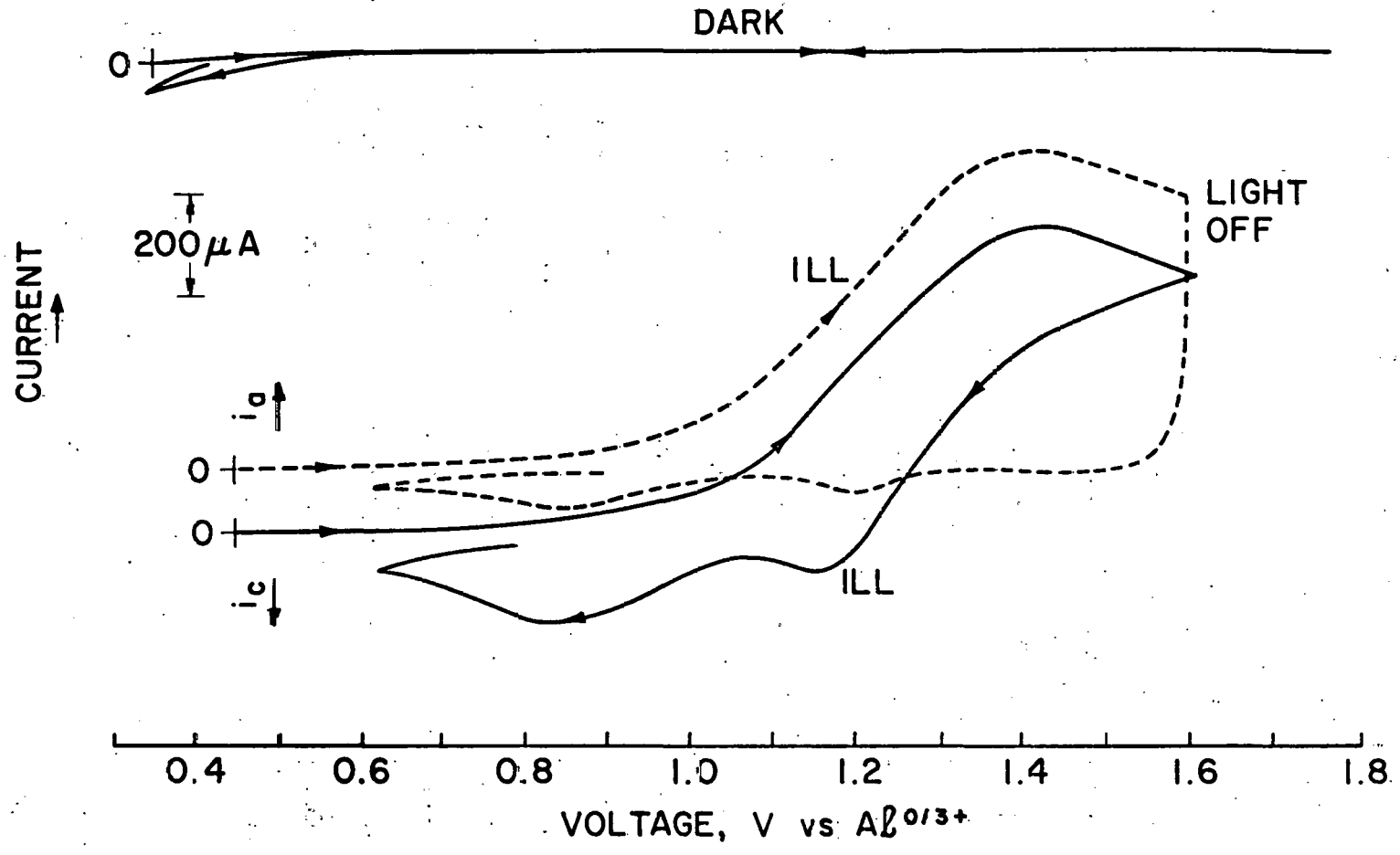

and dication stability. It is also noted that the presence of multiple 1-electron waves (rather than a single multi-electron wave) in the cyclic voltammograms suggests that surface states may be mediating the back electron transfer in this cases as discussed by previous authors [17]. If this is indeed the case, a second set of states situated very close to the valence band edge in n-GaAs is implicated by the present data. Further studies aimed at elucidating these aspects are in progress in this laboratory.

Linear Sweep Voltammetry on n-GaAs

Linear sweep voltammograms were obtained on n-GaAs electrodes in the dark and under illumination. Both neat $A\ell C\ell_3$-BPC electrolytes and $A\ell C\ell_3$-BPC/toluene mixtures were utilized for these studies. The electrolytes were magnetically studied to facilitate diffusion of electroactive species away from the n-GaAs surface. In all cases, the dark anodic current flow was negligible. Photocurrents were observed to flow at potentials quite positive of the flat-band level and showed the usual light intensity dependent plateau. A two- to three-fold increase in current densities was observed for the $A\ell C\ell_3$-BPC/toluene mixtures relative to the neat liquids. This observation is consistent with the increase in the conductivity and viscosity noted by previous authors on addition of organic solvents [10]. A representative set of data is shown for HMB in Figure 7. The current densities at short-circuit conditions and the voltage output (defined as the difference between the onset potential and the equilibrium value on carbon), are assembled in Table 3 for the various hydrocarbons. These output parameters were stable for periods up to $\sim$ 2 hours. No visible damage to the n-GaAs surface was noted at the conclusion of these experiments. Long-term stability, however, remains to be demonstrated.

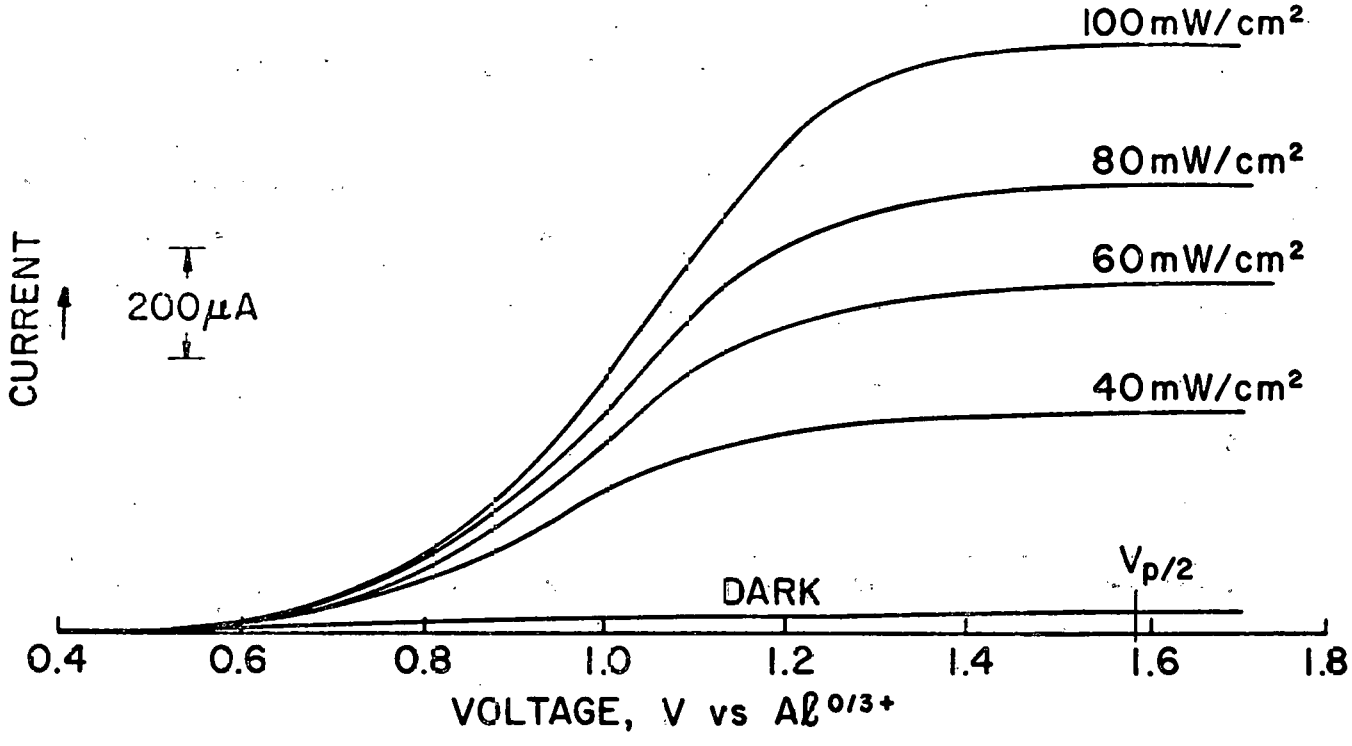

Figure 7: Linear sweep voltammograms in n-GaAs in the $A\ell Cl_3$-BPC/toluene 50 v/v mixture containing hexamethyl benzene. Scan rate: 200 mV/sec.

TABLE 3

Linear Sweep Voltammetry on Illuminated n-GaAs Electrodes[a)]

in $A\ell Cl_3$-BPC/toluene Electrolytes (50 v/v solutions)

Species	Onset Potential V vs. $A\ell^{0/3+}$	$V_{1/2}$ V vs. $A\ell^{0/3+}$	Open-Circuit Voltage[d)] V	Short-Circuit Current Density mA/cm^2
BP	0	+1.06	1.06	0.05
DPA	+0.1	+1.15	1.05	0.19
A	-0.2	+1.19	1.39	0.26
HMB	+0.5	+1.59[c)]	1.09	4.16

A) Light intensity: 100 mW/cm^2; scan rate: 200 mV/sec.

b) Determined by cyclic voltammetry.

c) The value refers to $V_{p/2}$ (cf., Table 1)

d) Taken as the difference between the onset potential and $V_{1/2}$.

3. PHOTOELECTROCHEMICAL CHARACTERIZATION OF CdSe THIN-FILM ELECTRODES IN AQUEOUS ELECTROLYTES

EXPERIMENTAL

Thin films of CdSe on titanium foil substrates were prepared at the Indian Institute of Technology, New Delhi, by the overall chemical reaction:

$$Cd(NH_3)_4^{2+} + SeSO_3^{2-} + 2\ OH^- \rightarrow CdSe + 4NH_3 + SO_4^{2} + H_2O \qquad (2)$$

Relevant details on the growth of these films are given elsewhere [18,19]. The films labeled "Film 1, 2 and 3" were prepared at 85°C with 2.1, 2.8 and 3.5 M NH_3 concentrations and had thicknesses ~0.7, 0.85 and 0.9 μm respectively. The as-grown films were n-type with resistivity ~10^7 - 10^8 Ω-cm. On annealing at 280°C for 30 min in vacuum (10^{-5} Torr), the resistivity was brought down to the range 1-10 Ω-cm. The annealed films had carrier concentrations in the range $5x10^{17}$- $5x10^{18}$ cm^{-3}, and carrier mobilities in the range 1-10 cm^2/V-sec.

Electrode fabrication consisted of cutting the 3x4 cm^2 as-prepared sheets of thin films into small wafers of area in the range, 0.15 - 0.5 cm^2. The CdSe film was scraped off from one side of the wafer and a back contact was made to the exposed titanium by application of conductive silver epoxy. A Teflon-coated copper wire was attached to the back contact by using the same epoxy. The entire back surface and edges of the electrodes were then covered with nonconducting epoxy resin.

A mixture of solutions of 1M Na_2S, 1MS and 1M NaOH in deionized water was used as the electroltye in the PEC cells. The cells were continually purged with a slow stream of pre-purified argon gas. Both

two-electrode and three-electrode PEC configurations were employed. A vitreous carbon plate (1.5 x 15 x 30 mm, Atomergic Chemetals Corp., N.Y.) was used as the counter-electrode in both cases. A saturated calomel electrode (SCE) was used as the reference electrode for potentiostatic measurements.

Two types of etching were employed for the CdSe thin film photoanodes, prior to their use in the PEC cells: a chemical etch consisting of successive non-convective dips in 6M, 1M and 0.1M HCℓ for 3-5 sec followed by a rinse in deionized water, and a photo-etch according to the procedure described by a previous author [20] wherein, the photoelectrode is illuminated under short-circuit conditions in a dilute aqueous acid solution, for example 0.1M HCℓ.

Current-voltage measurements

Figures 8-10 illustrate the current-voltage behavior of PEC cells based on solution-grown CdSe thin films. These data were obtained on two-terminal devices although no significant differences in behavior were observed in the potentiostatic mode with three-electrode PEC cells. Polarization effects at the counter-electrode (vide supra) can be therefore ignored in the following discussion. Open circuit potentials (V_{oc}) in the range 0.20-0.26 V, short-circuit current densities (J_{sc}) ranging from 0.1 to 2 mA/cm^2 and fill-factors spanning the range 0.20-0.35 were observed for the various devices depending on the prior thermal treatment of the film and surface preparation. Table 4 summarizes the performance parameters for the various PEC devices tested in the present study. In general, photo and chemical etching tends to improve the J_{sc} values and therefore the energy conversion efficiency of the device. Film #3 was found to yield better-quality electrodes than Films #1 and

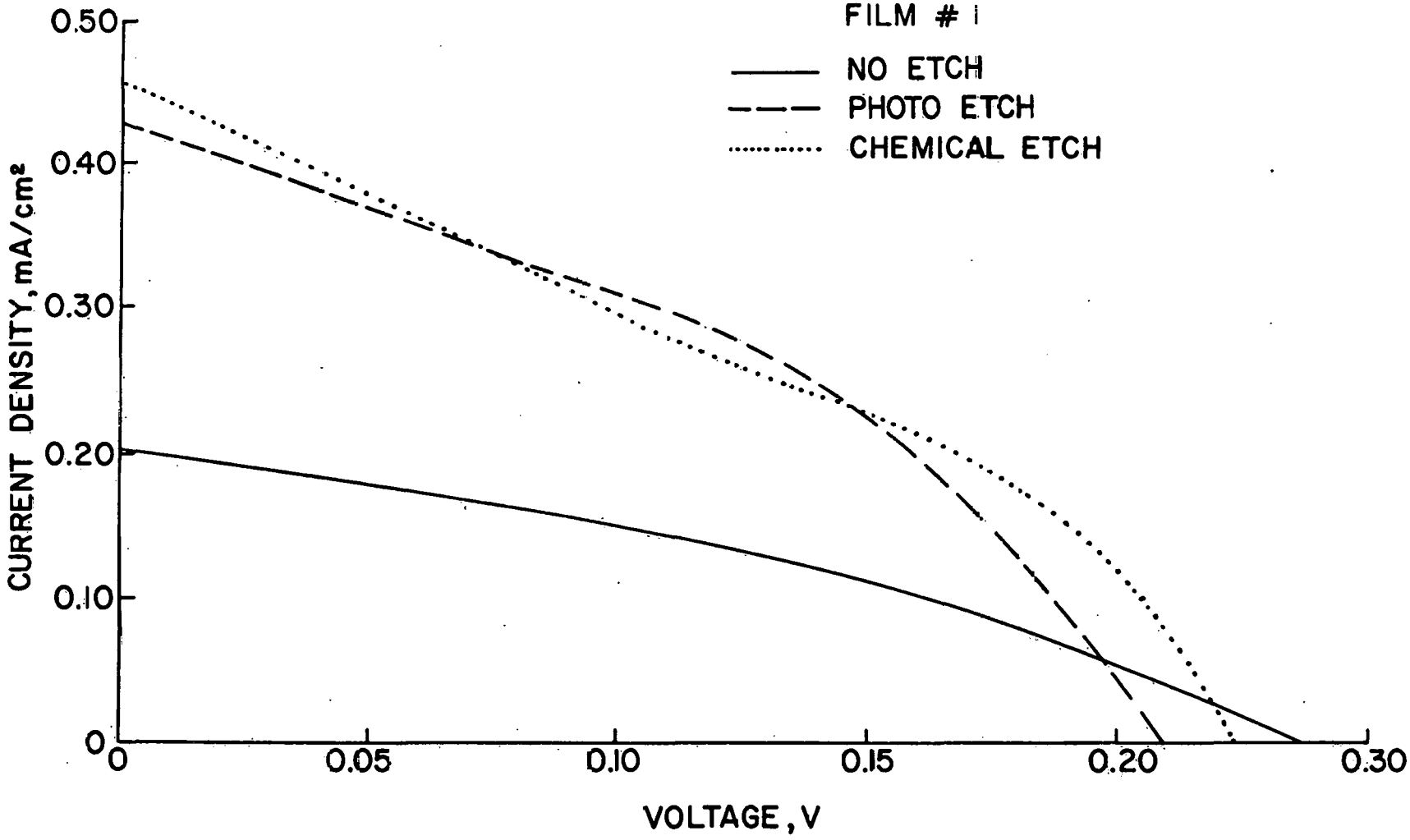

Figure 8: Photocurrent-voltage curves for solution-grown CdSe photoanodes (Film #1). Light source: Tungsten-halogen lamp, light intensity: 100 mW/cm^2.

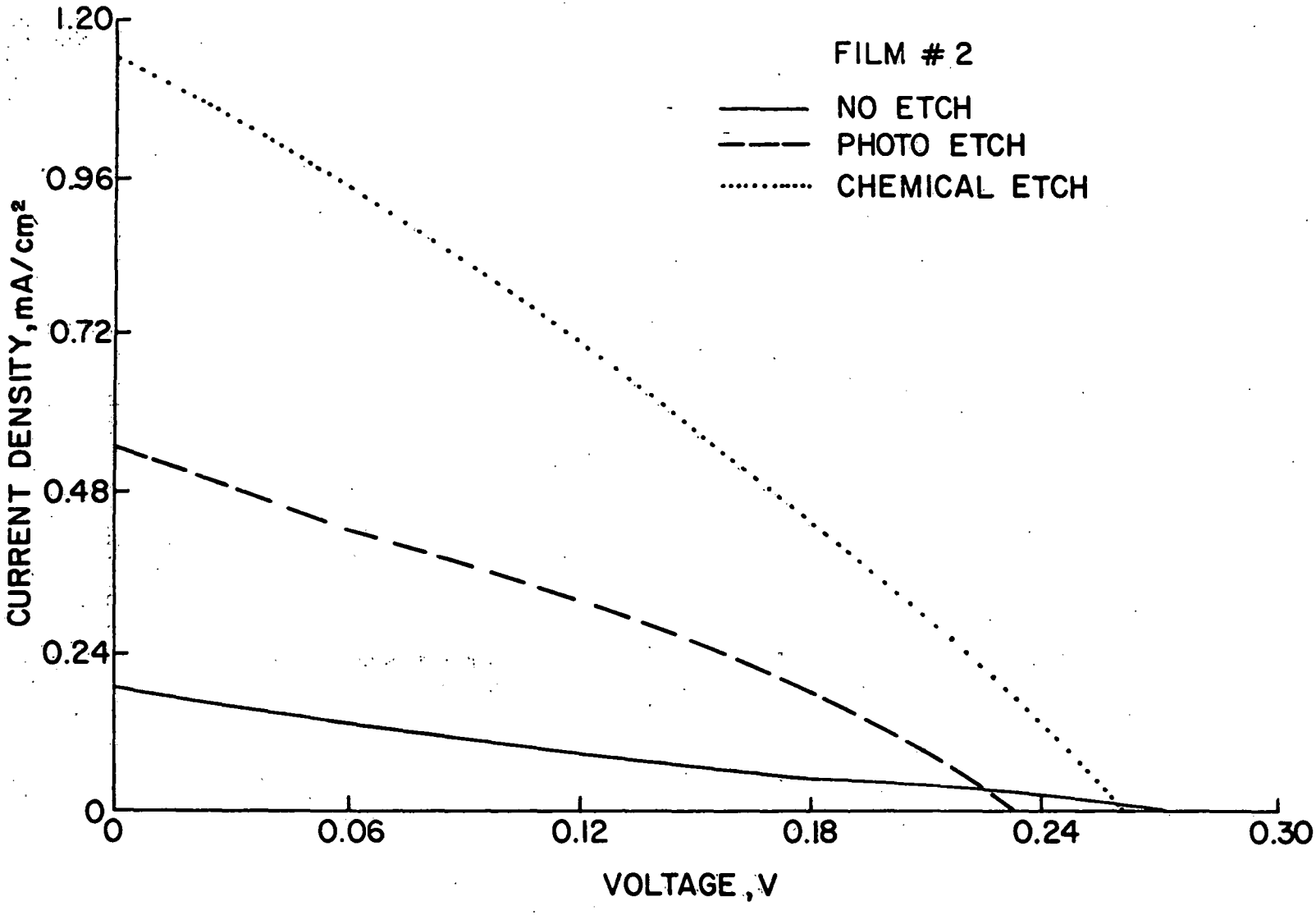

Figure 9: Photocurrent-voltage curves for solution-grown CdSe photoanodes (Film #2). Light source and intensity same as in Figure 8.

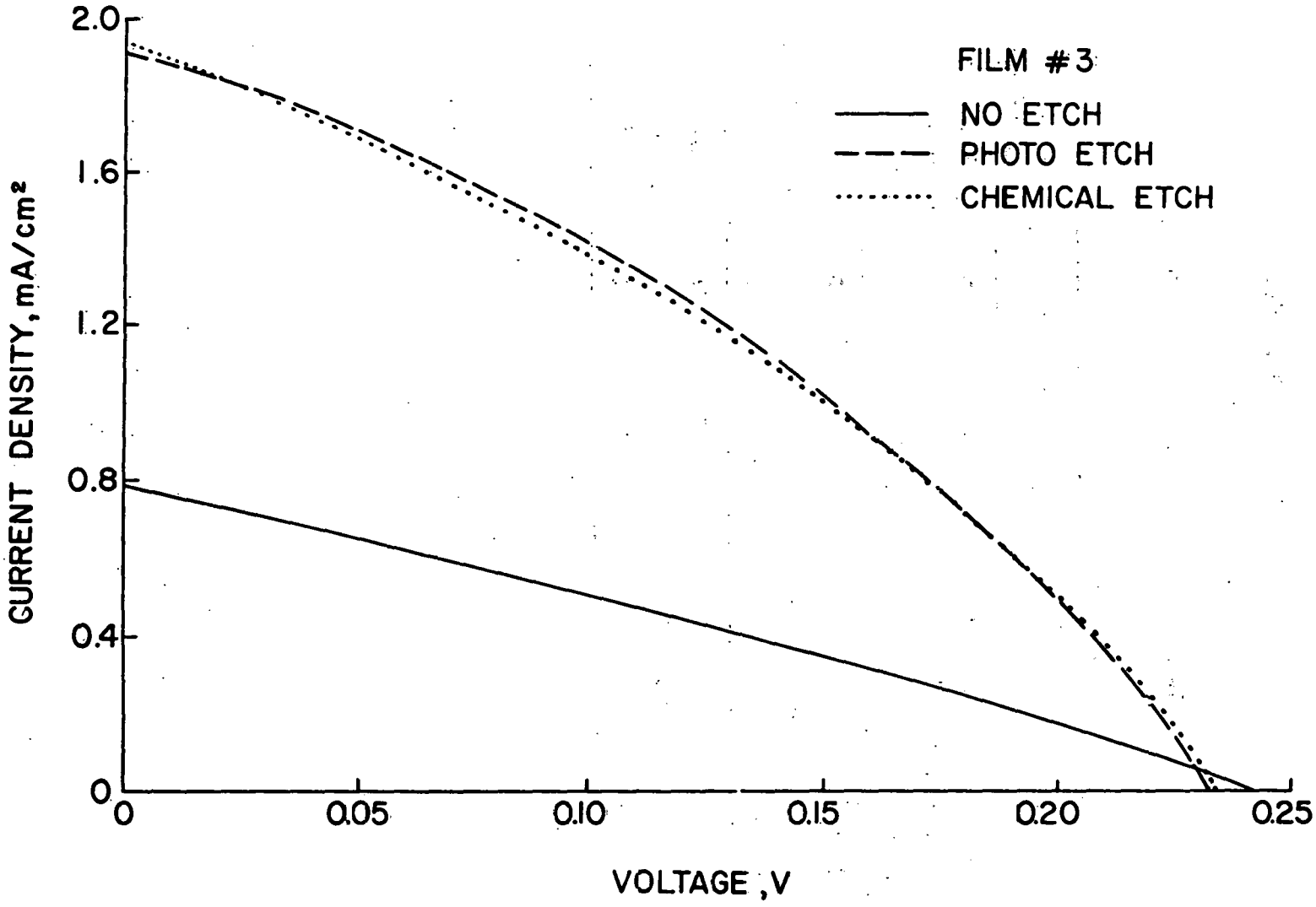

Figure 10 : Photocurrent-voltage curves for solution-grown CdSe photoanodes (Film #3). Light source and intensity same as in Figure 8

Table 4

Performance parameters of PEC devices based on solution-grown CdSe thin films.

(Light intensity: 100 mW/cm^2, electrolyte: 1MS, 1M Na_2S, 1M NaOH)

Film No.	Prior Treatment	V_{oc} V	J_{sc} mA/cm^2	FF	Conversion Efficiency %
	None	0.28	0.21	0.35	0.021
1	Chemical etch	0.25	0.47	0.33	0.039
	Photo-etch	0.22	0.44	0.38	0.037
	None	0.28	0.20	0.20	0.011
2	Chemical etch	0.25	0.56	0.23	0.032
	Photo-etch	0.23	1.17	0.29	0.078
	None	0.24	0.78	0.27	0.051
3	Chemical etch	0.23	1.92	0.34	0.150
	Photo-etch	0.23	1.90	0.34	0.149

#2 (Table 4) as expected from thickness considerations (vide supra). No attempt was made in these experiments to optimize cell geometry, redox concentration, etc. since the main objective of this work was to characterize the overall photoelectrochemical behavior of solution-grown CdSe thin films. However, by using suitably recrystalized and etched CdSe film deposited on SnO_x:F coated glass substrates, V_{oc} values in the range 0.40 - 0.62 V, J_{sc} up to 6 mA/cm^2 (50 mW/cm^2 light intensity) and fill factors as high as 0.50 have been obtained. The details of these prior treatments and the performance of the corresponding PEC cells are reported elsewhere [21].

Figure 11 compares the current-voltage behavior in the dark and under illumination for Film #3. These data were obtained under potentiostatic conditions. Similar behavior was observed for Films #1 and #2. The usual rectification behavior expected in the reverse bias regime for semiconductor/electrolyte junctions in the dark is observed here. From Figure 11 and similar data for the other films, the flat-band potential (V_{fb}) is seen to be more negative than ca. - 1.0 V (vs SCE) in the polysulfide solution. A more precise location of the V_{fb} value is obtained from the electrical impedance measurements described below.

A feature worthy of note in the data shown in Figure 11 is the gradual increase in current with increasing reverse bias in the dark. This increase is particularly pronounced on illumination of the device. At voltages significantly anodic of ca. 0.5 V (vs SCE), a very rapid increase in current (not shown in Figure 11) was noted for all the films examined in the present study. This behavior is commonly encountered in solid-state devices and is attributed to dielectric breakdown [22]. The gradual increase in current prior to this abrupt change, however, is of

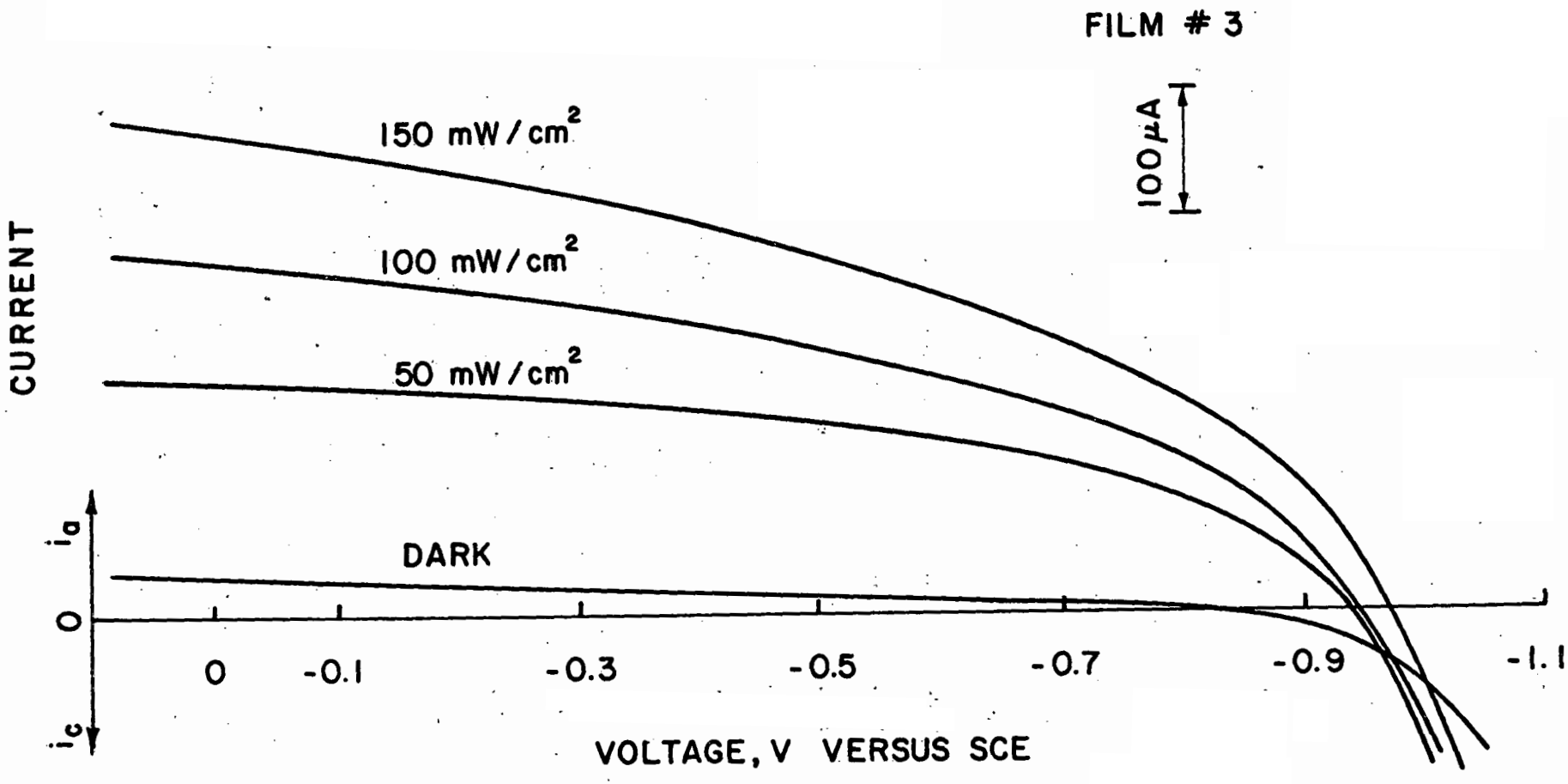

Figure 11: Potentiostatic current-voltage curves in the dark and under illumination for solution-grown CdSe photoanodes (Film #3).

more relevance to this study. There are three possible explanations for this "anomalous" behavior: (a) in the reverse bias direction, the presence of an interfacial layer causes the effective barrier height to decrease with increasing bias, so that the reverse current does not saturate [22], (b) hole-electron pairs are thermally generated in the depletion region under conditions of large reverse bias (i.e., large band-bending in the semiconductor), and (c) the current increases due to the onset of electron injection from the electrolyte because the barrier becomes thin enough for tunneling to take place.

Of the above possibilities, we prefer the explanations based on (a) and (c) above. Support for (a) derives from observations [23-25] on the formation of a thin CdS layer on the surface of the CdSe electrodes by S/Se substitution. On the other hand, the more pronounced increase in the currents in the reverse bias direction on illumination relative to the dark case (Figure11), suggests that the tunneling process (i.e., electron injection from the electrolyte) might be enhanced because of the slight increase in the majority carrier density at the interface. Under potentiostatic conditions such as those employed for the measurements in Figure 11. this is equivalent to heavier doping of the semiconductor and hence a thinner surface barrier.

A more detailed discussion of the current-voltage characteristics and the effect of interfacial layers is postponed to a later section.

Effect of light intensity

If we model the semiconductor/electrolyte interface as a Schottky barrier, it is possible to represent the current-voltage characteristic by the following expression [26]:

$$J = J_{ph} - J_d = J_{ph} - J_o \, [\exp (q\,V/nkT) - 1) \qquad (3)$$

Here J is the net current density (current per unit area), J_{ph} and J_d are the photocurrent density and dark current density respectively, J_o is the reverse saturation current density, V is the voltage, n is the "junction-ideality" factor and other terms have their usual significance. For bias voltages exceeding 3 kT/q, we can neglect the last term in the bracket in Equation 3. Also at equilibrium (open-circuit conditions), $J_{ph} = J_d$ and $V = V_{oc}$ so that rearrangement of Equation 3 yields:

$$V_{oc} \cong \frac{nkT}{q} \ell n \frac{J_{sc}}{J_o} \tag{4}$$

where V_{oc} is the open-circuit voltage and J_{sc} is the short-circuit current density. If we further assume that $J_{sc} \alpha \underline{I_L}$ (= incident light intensity) and $J_{sc} >> J_o$, Equation 4 reduces to the following expression:

$$V_{oc} \alpha \frac{nkT}{q} \ell n I_L \tag{5}$$

A plot of V_{oc} against $\ell n I_L$ should yield a straight line from which values of n may be determined for the particular device. An ideal device should have an n value of unity so that the slope of a straight line plot of V_{oc} versus log I_L should be ca. 60 mV. Figure 12 illustrates such plots for CdSe films #1, 2 and 3. An alternative method involves plotting V_{oc} versus log J_{sc} (cf., Equation 4). The slopes determined by these analyses are assembled in Table 5. The magnitudes of these slopes can be rationalized only if $n \simeq 2$.

The above assumption that J_{sc} is directly proportional to the light intensity, is borne out by the data shown in Figure 13. The linear

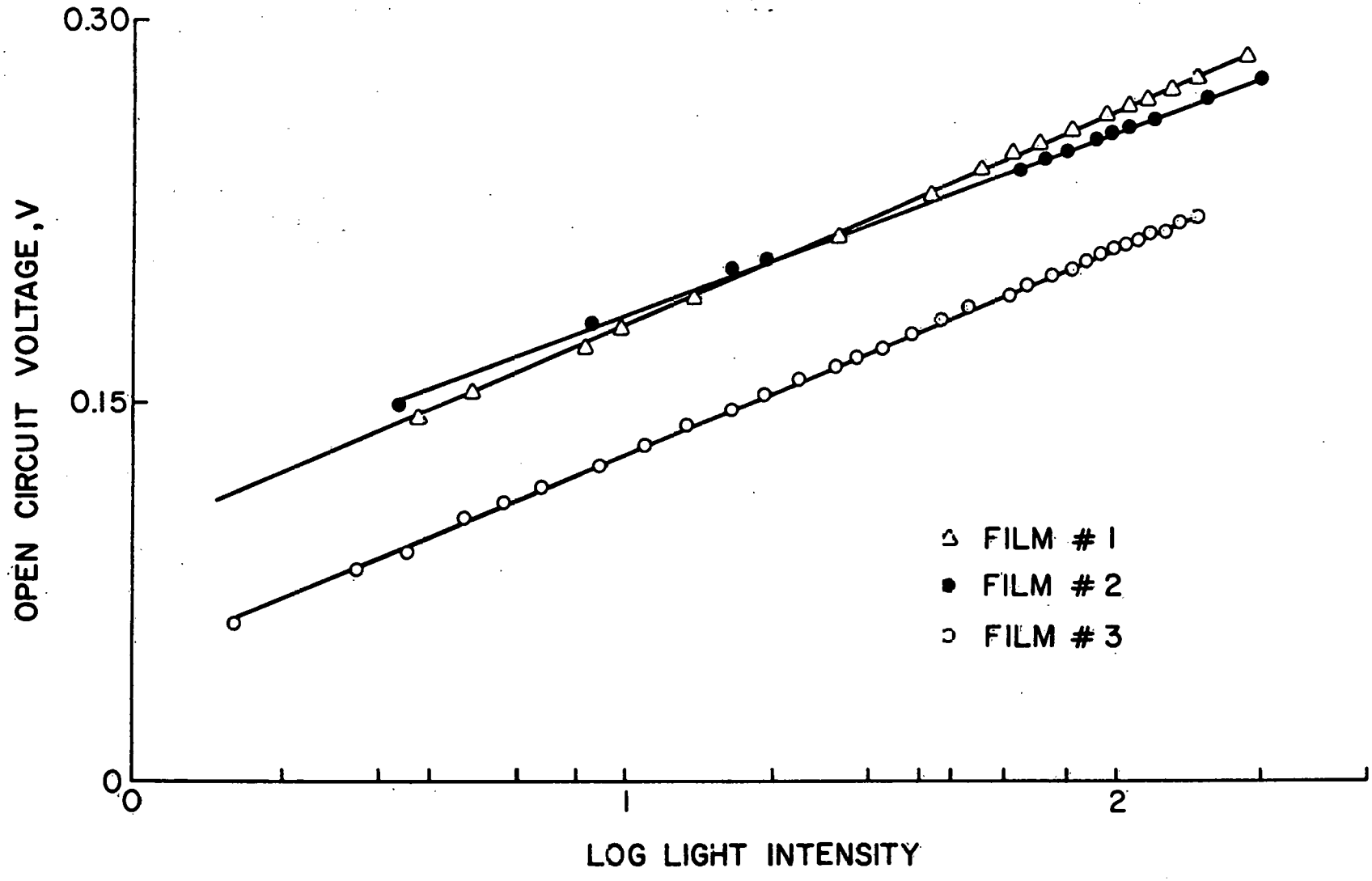

Figure 12: Plots of open-circuit voltage versus log light intensity for solution-grown CdSe photoanodes.

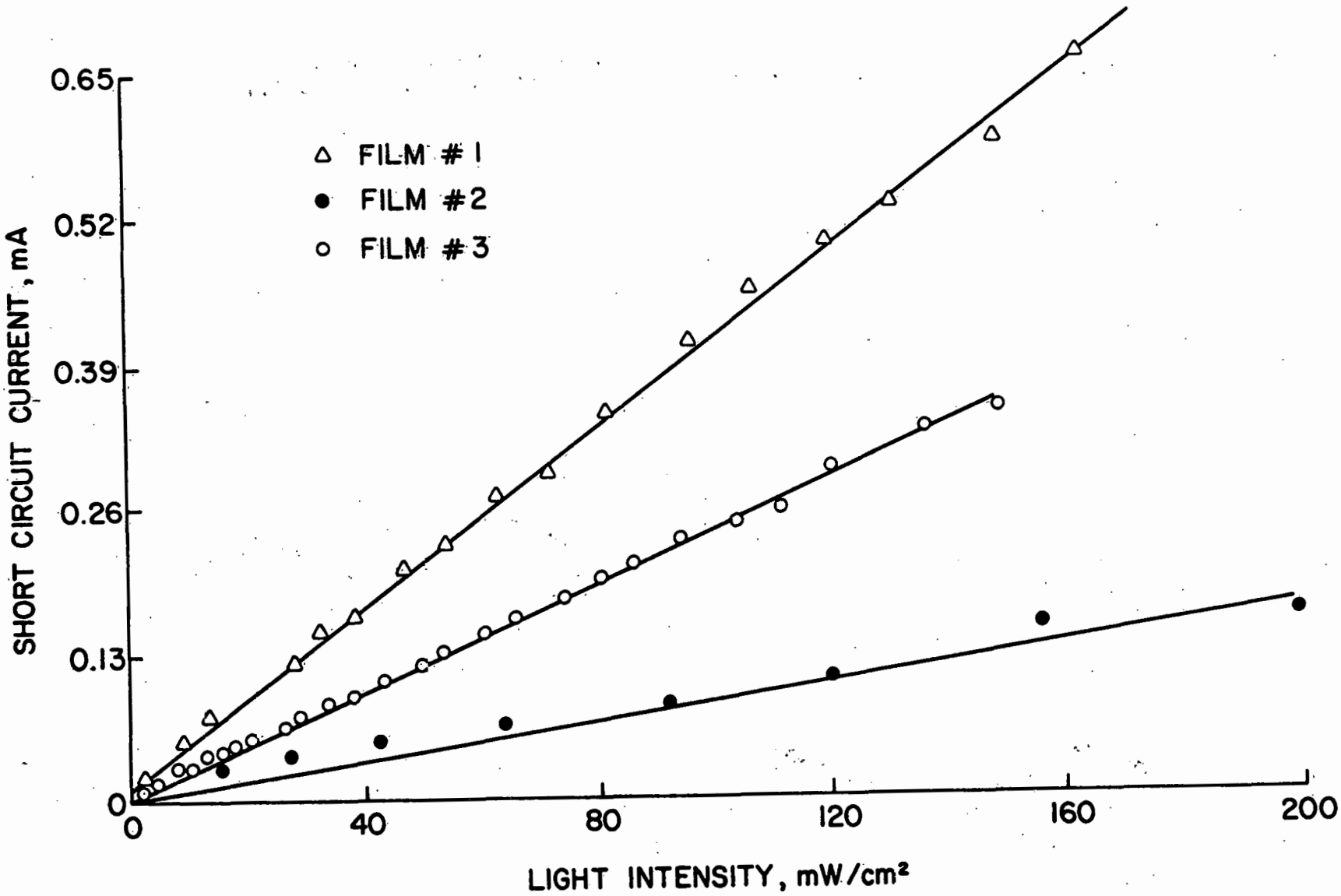

Figure 13: Dependence of short-circuit current density on light intensity for solution-grown CdSe photoanodes.

Table 5

Junction ideality factors for the illuminated CdSe/electrolyte interface.

Method of Determination	Slope (V)			n		
	Film #1	Film #2	Film #3	Film #1	Film #2	Film #3
V_{oc} versus log J_{sc}	0.120	0.108	0.107	2.03	1.83	1.81
V_{oc} versus log I_L (c.f. Eq. 4)	0.108	0.130	0.115	1.83	2.20	1.95

dependence also demonstrates that transport of electro-active S^{2-} species to the CdSe/electrolyte interface is not limiting the rate of the overall charge-transfer reaction over the range of light intensities employed in this study.

The functional dependence of J_{sc} and V_{oc} on light intensity for CdSe-based PEC cells was noted by previous authors in studies on single crystals [27] and on thin films prepared by vacuum evaporation [28].

Photocurrent-wavelength measurements

Figure 14 illustrates the spectral response of solution-grown CdSe thin film electrodes in polysulfide solution. The sharp decrease in response below ~520 nm is consistent with the increased absorption of polysulfide solutions below these wavelengths [27,29]. The long wavelength cut-off is less sharp relative to the behavior of single crystal electodes [28] and reflects the non-optimized thickness of the present CdSe films leading to a consequent deterioration in long wavelength response. The gradual decrease in photoresponse into the short-wavelength region is indicative of surface recombination of photogenerated minority carriers presumably mediated by electronic states in the band-gap (cf., Refs. [30], [31]). Application of reverse bias to the electrode results in the expected increase in photocurrents arising from better field separation of photogenerated carriers although the surface recombination component is not significantly reduced (Figure 14).

Equivalent circuit-representation

Equivalent circuit representation of the semiconductor/electrolyte interface [20,21] enables identification of specific components of the overall electrical network, that are responsive to potential and current pertubations. Figures 15a, b, c and d illustrate successive reductions

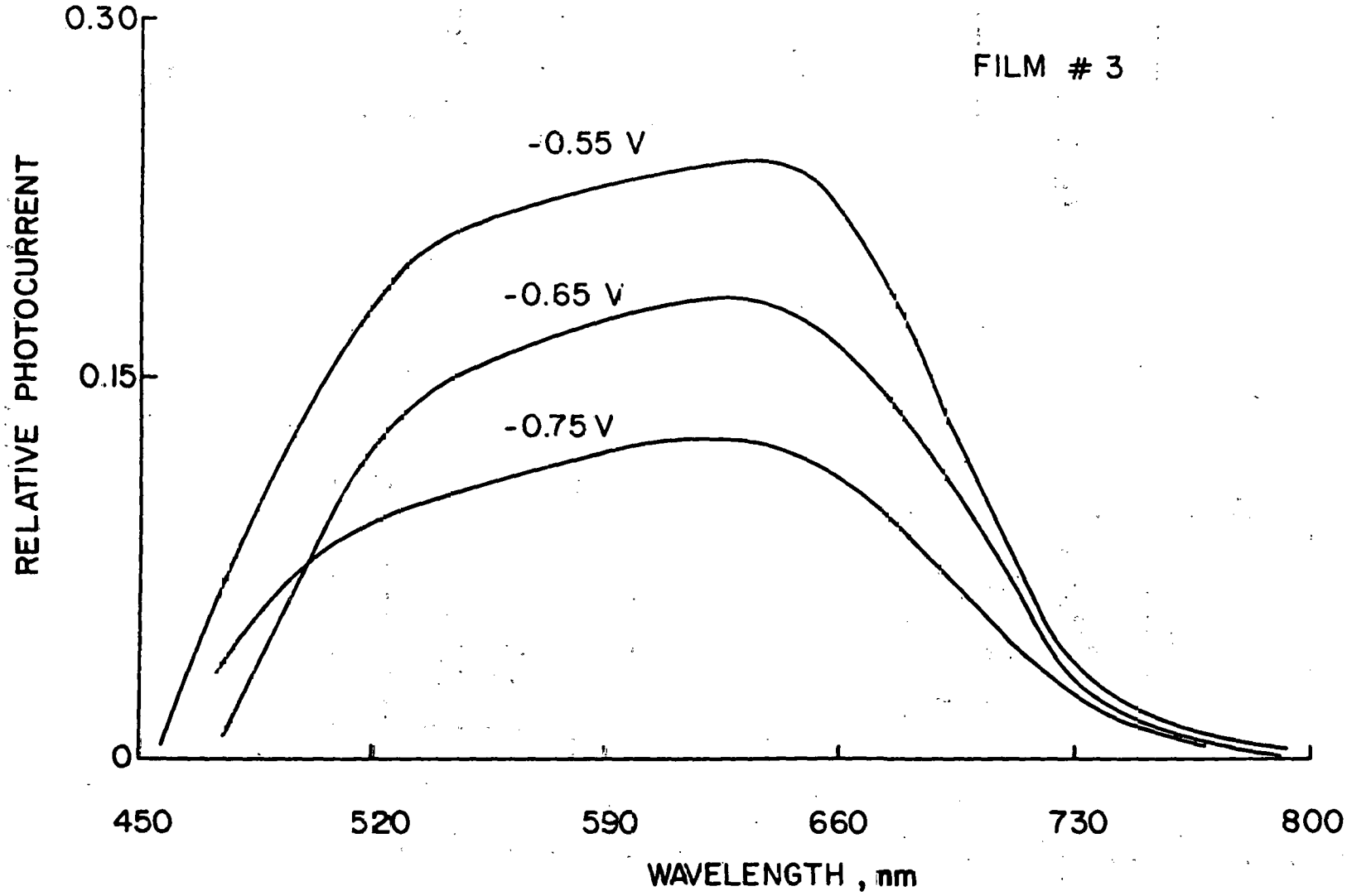

Figure 14: Photocurrent-wavelength characteristics for solution-grown CdSe photoanodes (Film #3) at various values of reverse bias. The voltages refer to SCE reference electrode. The photoresponse was normalized to take into account, variations in intensity and quantum flux with wavelength.

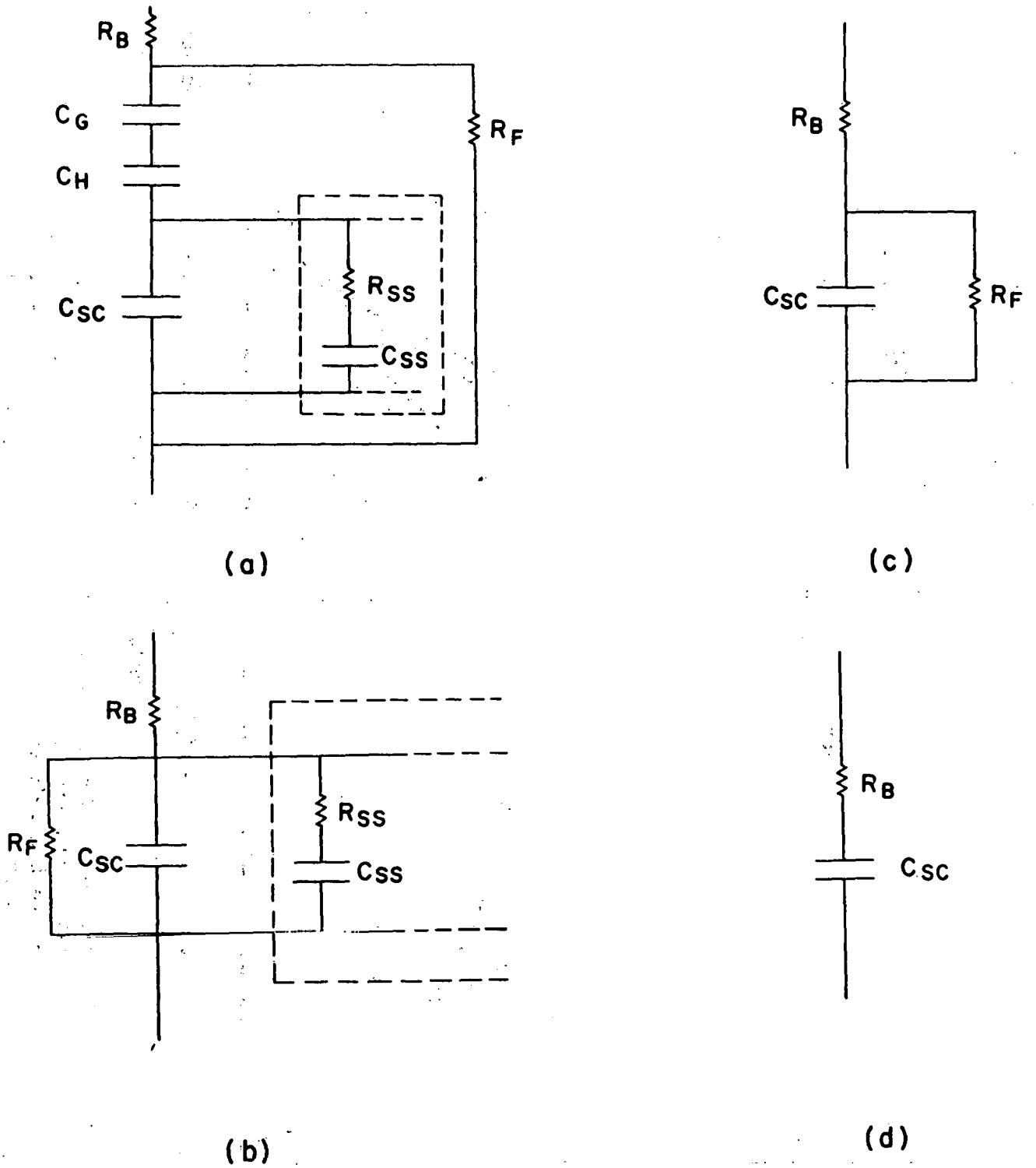

Figure 15: Equivalent circuit representations of the semiconductor/electrolyte interface. Figures 10a, b, c and d show successive reductions in the complexity of the electrical network. See text for description of symbols.

of the equivalent circuit for a model semiconductor/electrolyte interface leading to the highly idealized system shown in Figure 15d. Here C_{sc} is the space-charge capacitance, C_H is the Helmholtz layer capacitance, C_G is the Gouy layer capacitance, R_B is the internal series resistance comprising the contributions from the electrolyte, bulk semiconductor and the back ohmic contact, R_F is the resistance associated with Faradaic charge-transfer processes at the interface and C_{SS} and R_{SS} are the capacitance and resistance terms arising from surface states or traps at the interface. For an ideal device, C_G and C_H should be large relative to C_{sc}, R_B should be small, R_F should be large and surface-state effects should be absent or at least minimal. In concentrated electrolytes such as those employed in the present study, the C_G term may be ignored and since usually $C_H >> C_{sc}$, an expression for the parallel admittance may be derived [32] (cf., Figure15c):

$$\omega C_p = \frac{(G_B + G_F)(\omega G_B C_{SC}) - \omega G_B G_F C_{SC}}{(G_B + G_F)^2 + (\omega C_{sc})^2} \qquad (6)$$

and

$$G_{p/\omega} = \frac{(G_B G_F/\omega)(G_B + G_F) + G_B \omega C_{SC}^2}{(G_B + G_F)^2 + (\omega C_{SC})^2} \qquad (7)$$

It is noted that in the above, effects from surface states have not been taken into account <u>per se</u>. The conductance terms G (= 1/R) have been employed in the above expressions in place of resistances, since the measured quantity here is the parallel conductance.

Each C-G combination above causes a peak in $G_{p/\omega}$ versus ω curves. Unless the G_F term becomes very large, it will not overlap

the peak that is caused by the C_{sc} - G_B combination. The more ideally polarized the interface, the smaller is the G_B term and hence the lower the frequency range at which it will have an appreciable effects. For very low frequencies ($\omega \to 0$) and for $G_B >> G_F$, $G_p \simeq G_F$. Typical $G_{p/\omega}$ versus ω curves are shown in Figures 16 and 17 for Films #1 and #3 respectively. Values for C_{sc} and R_B can be determined from these data from the expressions [33,32]:

$$C_{sc} = 2[G_{p/\omega}]_{max} \tag{8}$$

$$R_B = 1/G_B = 1/(2\ \omega\ [G_{p/\omega}]_{max}) \tag{9}$$

G_F (or R_F) is given by the extrapolated value of the low-frequency data to the $G_{p/\omega}$ axis (cf., Figures 16 and 17). Values of C_{sc}, R_B and R_F thus determined and the overall circuit for the CdSe/electrolyte interface are shown in the inset of Figures 16 and 17. The solid circles in Figures 16 and 17 represent experimental data; the lines are "theoretical" curves based upon calculated values of the circuit elements. Computational procedures for data fitting and other relevant details may be found elsewhere [32].

It is again noted that the circuit representations in Figures 16 and 17 for the CdSe/electrolyte interface are somewhat idealized since surface state effects have been ignored. Based on previous measurements in this laboratory on the n-GaAs/molten-salt electrolyte interface, the discrepancy between the theoretical curves and the experimental data in the intermediate frequency regime in Figures 16 and 17 may be attributed to the influence of surface states. Attempts to include this effect in computation of the theoretical $G_{p/\omega}$ curves were not entirely successful because adequate resolution of peaks arising from C_{ss} - G_{ss}

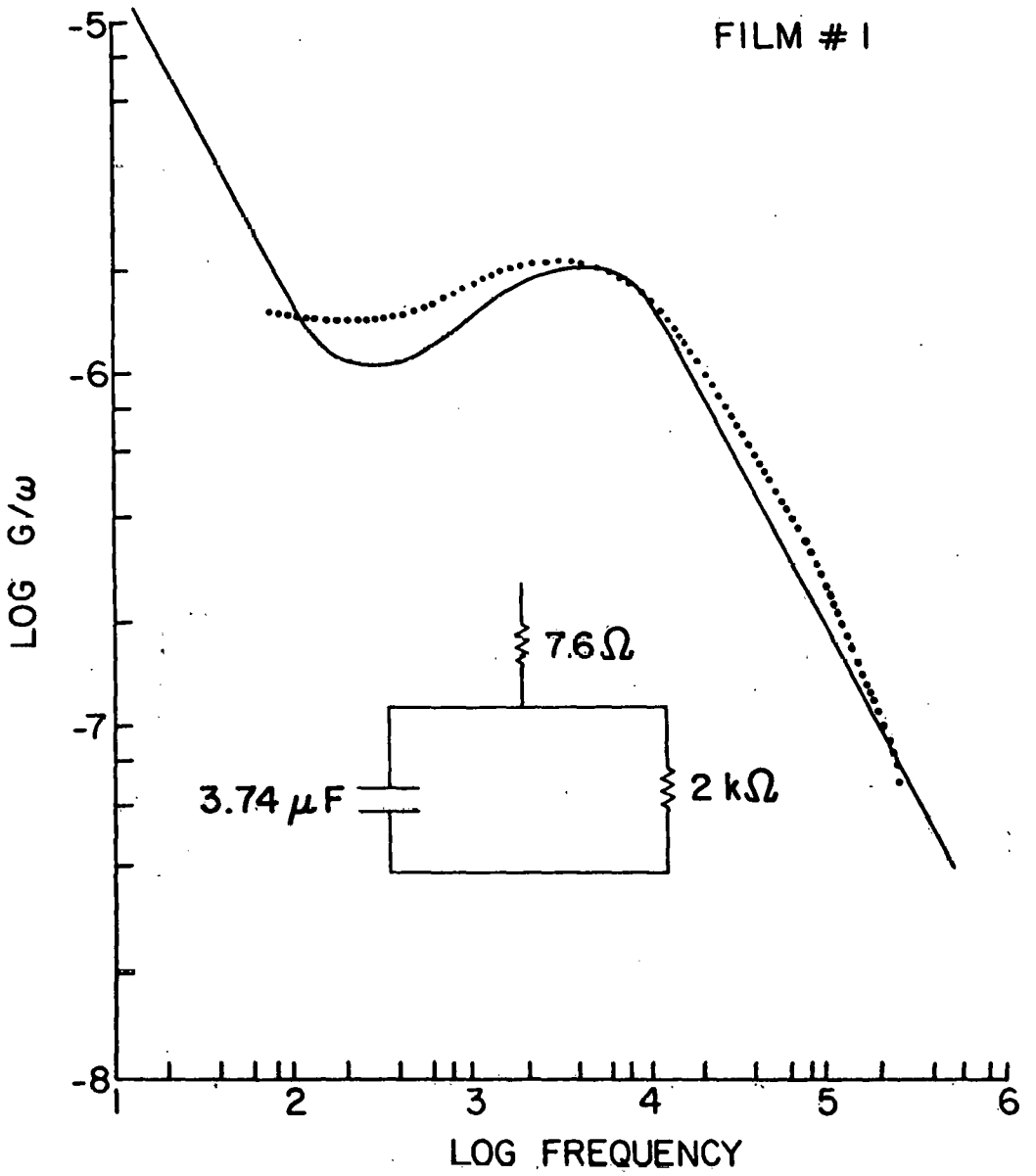

Figure 16: Impedance spectra of solution-grown CdSe photoanodes (Film #1). Solid circles: experimental points, Line: theoretical curve based on the circuit elements shown in inset of the figure. Electrode potential: -0.75 V (versus SCE).

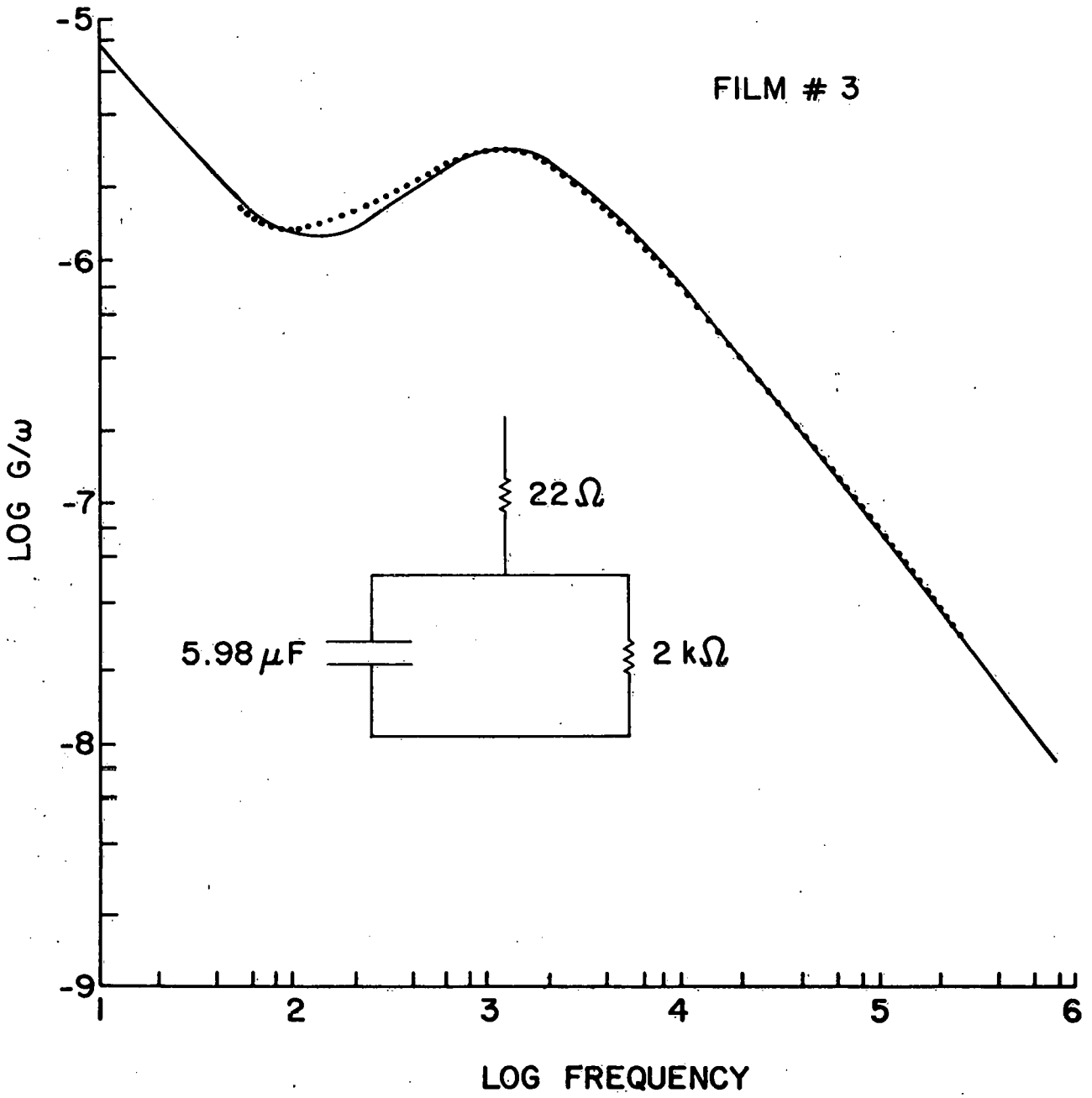

Figure 17: Impedance spectra of solution-grown CdSe photoanodes (Film #3). Description same as in Figure 11. Electrode potential: -0.80 V (versus SCE).

and C_{sc} - G_B combinations, was impeded by the shift of the C_{sc} - G_B peak toward lower frequencies relative to the GaAs case [14]. Either a decrease in G_B (with constant C_F) or an increase in C_{sc} (with constant G_B) can cause this shift [32].

The C_{sc} values computed from Equation 7 under conditions of varying bias may be utilized to determine V_{fb} values by the Mott-Schottky relationship [14]:

$$1/C_{sc}^2 = \frac{2}{q\,\varepsilon_s\,N_D\,A^2}\,(V - V_{fb} - kT/q) \qquad (10)$$

Here ε_s is the permittivity of the semiconductor, N_D is the semiconductor doping density and A is the electrode area. Figure 18 illustrates Mott-Schottky plots for Films #1 and #3. A V_{fb} value of -1.56 ± 0.06 V (versus SCE) was deduced from plots such as those shown in Figure 18 for the CdSe films examined in this study. This value pertains to that obtained in the polysulfide electrolyte and may be compared with values of -1.45 V, -1.34 V and -1.30 V (versus SCE) reported by previous authors for single crystal, vacuum-deposited thin films and for sintered pellets respectively [27,33]

GENERAL DISCUSSION

In a broad sense, the present data may be regarded as representative of the manner in which many analogous features in the electrical characteristics of the semiconductor/electrolyte junction and a Schottky barrier [24] may be utilized to assess the quality of the photoactive junction in a PEC electrode/electrolyte interface. For example, n values close to 2 have been observed for the present CdSe thin film electrodes (cf., Table 5). Values of n=2 are characteristic of the

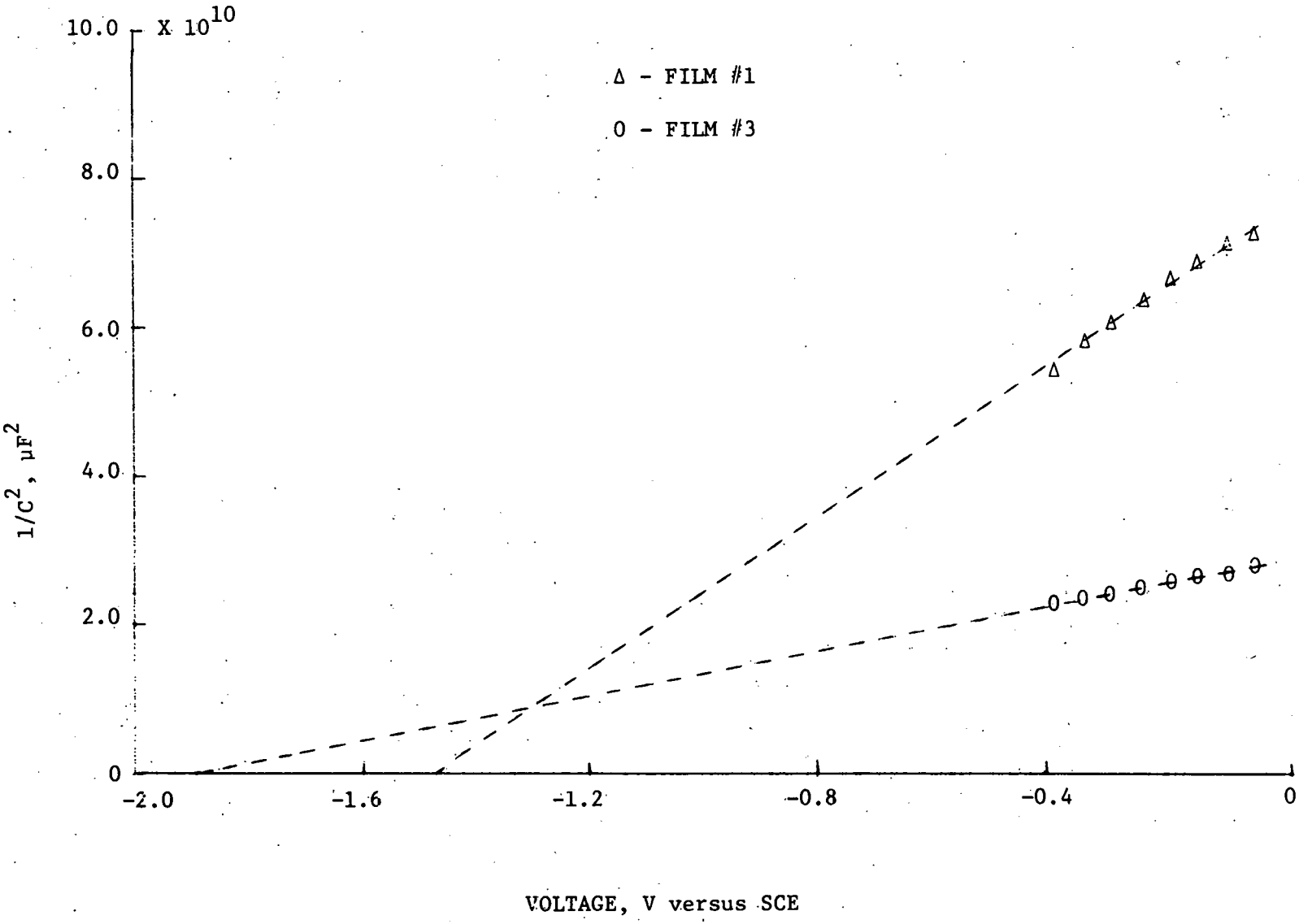

Figure 18 : Mott-Schottky plots for CdSe thin-film photoanodes (Films #1 and #3).

propensity of recombination processes involving photogenerated electron-hole pairs either at the semiconductor surface or in the depletion region [26]. This causes a deviation from the ideal current/voltage characteristic expecially at low values of applied bias. We postulate that a significant factor in this nonideal behavior is the presence of an ultrathin, tunnelable layer consisting of CdS on the CdSe surface (cf., Figure 19). This layer is believed to be electrically insulating because of compensation of excess Cd and/or Se vacancies [24]. The effect of this insulating layer on the photovoltaic characteristics of the CdSe/electrolyte junction is two-fold: (a) because of the potential drop across this layer, the zero-bias barrier height, ϕ_b° is lower than it would be in the absence of this layer (cf., Figure 19) and (b) when a bias is applied, part of the bias voltage is dropped across the CdS layer so that the barrier height, ϕ_b will be a function of bias voltage. The effect of this bias dependence of ϕ_b is to change the shape of the current/voltage characteristic in a manner represented by the inclusion of an ideality factor, n (cf., Equation 2).

The above effects may be represented by the expression [34]:

$$\phi_b = \phi_b^\circ - \alpha \left(2 q N_D/\varepsilon_s\right)^{1/2} \left(\phi_b - V - \Delta - \frac{kT}{q}\right)^{1/2} \qquad (11)$$

Here $\alpha = t\varepsilon_s/(\varepsilon_i + q\ t\ D_{ss})$, ε_i is the permittivity of the insulating layer, t is its thickness, D_{ss} is the surface state density, and Δ is the difference between that conduction band edge and the Fermi level.

Figure 19 illustrates the electrostatic aspects of the semiconductor/electrolyte interface in the presence of an ultrathin

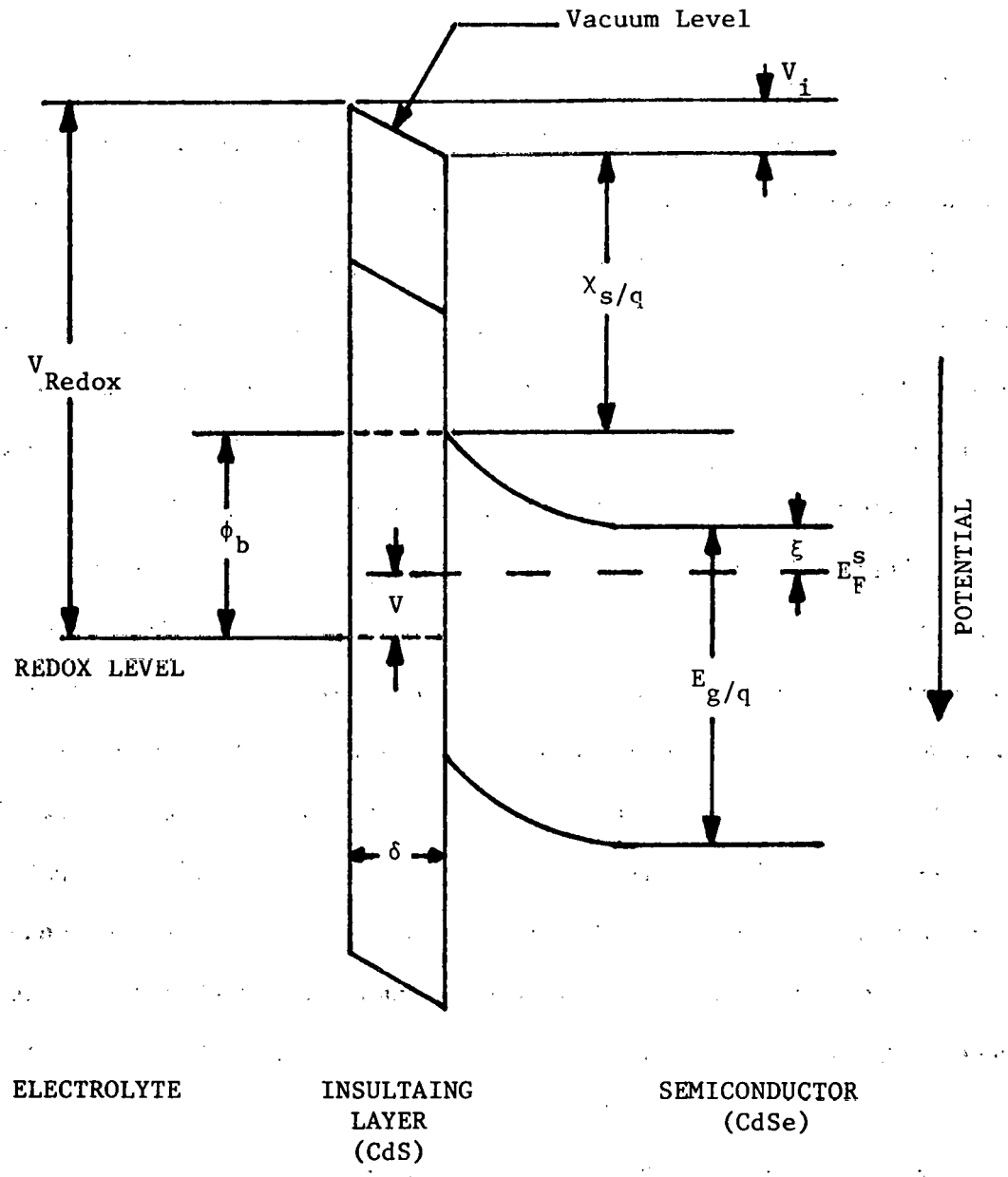

Figure 19 : Energy band diagram for the CdSe/electrolyte interface under any arbitrary forward bias. V_{redox} is the redox potential, χ_s is the semiconductor electron affinity, E_F^S is the Fermi level in the semiconductor and E_g is the energy band-gap in the semiconductor. Other symbols are defined in the text.

insulating layer. An estimate of the barrier-height lowering may be obtained from Equation 11, assuming $t = 20$ A°, $D_{ss} = 10^{17}$ eV^{-1} m^{-2}, $\varepsilon_s = \varepsilon_i \simeq 9\ \varepsilon_o$ [35] and $(\phi_b - V - \Delta + kT/q) \simeq 1$ V; a value $\phi_b° - \phi_b = 0.02$ V is obtained. This effect will be enhanced by a larger doping level in the semiconductor and a thicker insulating CdS layer. (Depth profiles reported by previous authors for CdSe photoelectrodes indicate a layer thickness of the order of 80 Å, Ref. 25 . The above value therefore is to be taken as a conservative estimate.) The barrier-height lowering would also be more pronounced under reverse bias because of the increase in the $(\phi_b - V - \Delta - kT/q)^{1/2}$ term in Equation 11.

The electrical impedence measurements illustrate the manner in which difficulties encountered in "conventional" capacitance measurements with frequency dispersion of C_{sc} values [36] may be avoided. Meaningful V_{fb} values may be extracted by utilizing the relationship of $G_{p/\omega}$ peak maxima with C_{sc} (cf., Equation 8). Indeed, capacitance measurements using the standard lock-in technique [1a] at discrete signal frequencies failed to yield reproducible Mott-Schottky plots for the present CdSe thin films. An additional advantage with the present approach is that changes in electrical conductance with voltage are much greater than corresponding variations in the capacitance [37], thereby enhancing the sensitivity of the technique. Further details of this new technique for measuring V_{fb} values are discussed in the next Section.

Work is continuing in these laboratories towards improvement of the surface quality of solution-grown CdSe thin films and thereby optimizing their performance in regenerative PEC devices for conversion of solar energy into electricity.

4. A NEW TECHNIQUE FOR THE DETERMINATION OF MOTT-SCHOTTKY PARAMETERS FROM ADMITTANCE MEASUREMENTS AND EQUIVALENT CIRCUIT MODELS

Background and Description of Technique

The central problem in the determination of V_{fb} and N_D from capacitance measurements lies in the method of relating the measured parameters to the elements comprising the semiconductor/electrolyte junction. These measured parameters may be based on either a series or a parallel combination of resistance and capacitance elements as shown in Figure 20. It is noted that these parameters are frequency dependent. On the other hand, the components in Figure 20 are passive elements and describe each individual electrophysical (e.g. spacecharge, surface states) or electrochemical (e.g. faradaic charge transfer) process in the system and their inter-relationships in terms of an overall electrical network. This network may take on varying degrees of complexity depending on the specific state of the electrolyte, semiconductor (bulk and surface) and the interface (Figure 20).

The measurement system has been described in previous papers from this laboratory [38,39] although a brief description follows for the sake of completeness.

The series or parallel components in Figure 1a are extracted from measurement of the attenuation or gain A, and the phase shift ϕ, of a small-amplitude ac signal which is superimposed on the applied bias voltage. These measurements are carried out with an automatic network analyzer and a frequency synthesizer such that the A and ϕ values are obtained over a continuous range of frequencies from 50 Hz to 1 MHz at a given bias voltage. Further details on the measurement system and calibration may be found elsewhere [32].

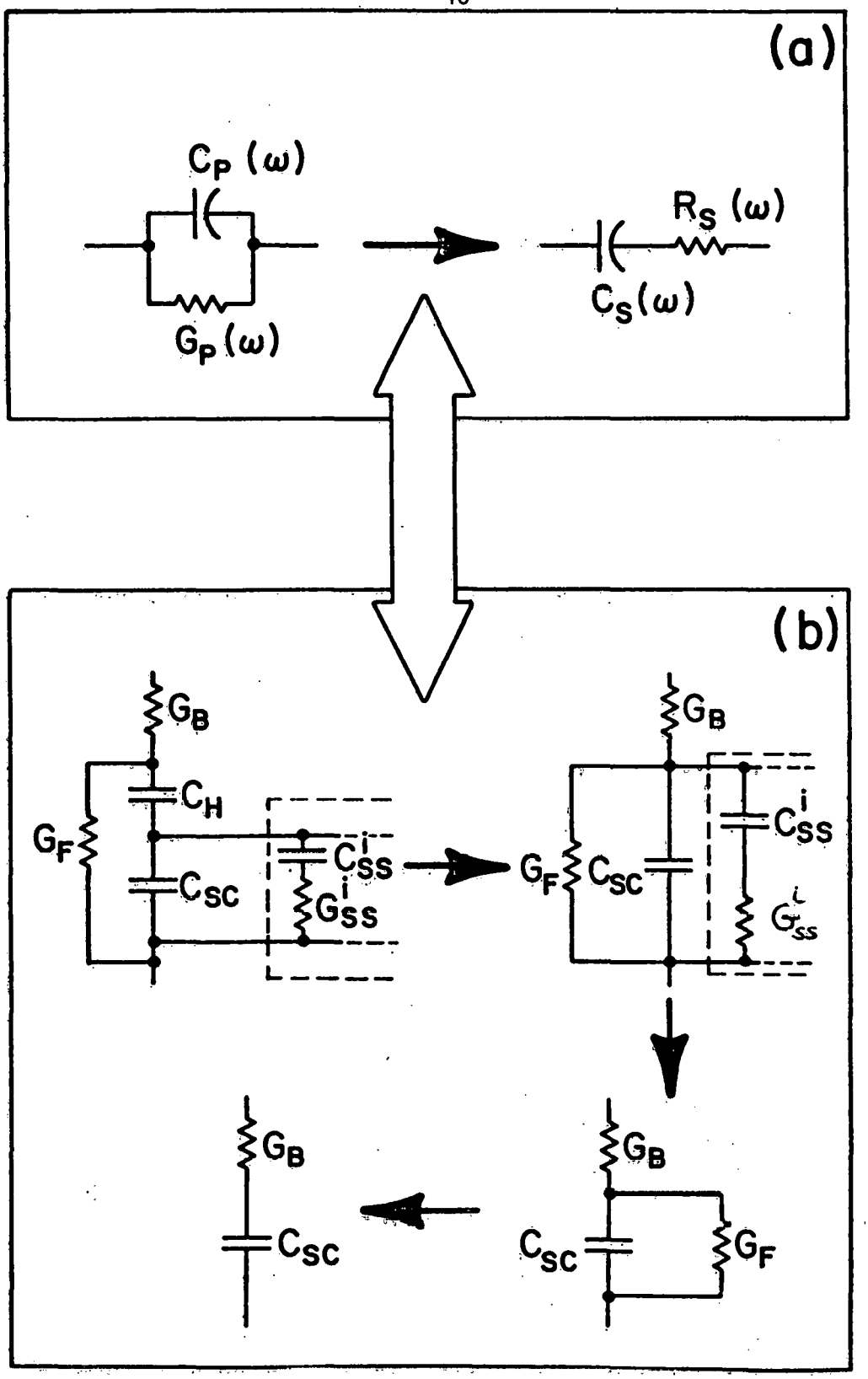

Figure 20: Experimentally measured quantitites for a semiconductor/electrolyte, C_p, G_p and their series equivalents.

The next step in the analysis is the representation of the measured frequency-dependent series or parallel elements (Figure 20) in terms of one of the network models shown in Figure 20. A step-by-step comparison of the data with network models of increasing complexity (c.f. Figure 20) is attempted until an adequate fit (vide infra) over the entire frequency range (at a given bias) is obtained [32,38,39].

The analytical procedures for extraction of the Mott-Schottky parameters are described in a subsequent section although it is noted here that the experimental conditions are so chosen that the Gouy layer capacitance, C_G (Figure 20) can be neglected. Additionally, the counterelectrode area is such that it is orders of magnitude larger than that of the working electrode. The measured capacitance therefore corresponds only to the semiconductor/electrolyte interface. The term G_B in Figure 20 contains primarily the contributions of the resistance of the bulk semiconductor, the bulk electrolyte and occasionally the metal/semiconductor ohmic contact.

To our knowledge, the only previous technique that bears some semblance to the one described herein, is that reported by Tomkiewicz [40, 41] It is stressed, however, that important differences exist in the methodology in the two cases. Tomkiewicz [41] utilizes high frequency measurements for the extraction of C_{sc} (C_{sc} = space charge capacitance, c.f. Figure 20). In our opinion, this approach has at least two handicaps: (a) the assumption that the high-frequency part of the curve can be represented as a single resistor and capacitor connected in series may not be valid in the presence of fast surface states and (b) the construction of a tangent to the high frequency portion of the curve seems arbitrary especially in view of the susceptibility of the data in this region to amplifier roll-off and other instrument limitations.

For Mott-Schottky analyses, the passive network element (c.f. Figure 20) of importance is the space-charge capacitance, C_{sc} [42]. It suffices, therefore, to consider the simplest representation of the semicondutor/electrolyte junction which consists of C_{sc} connected in series with the bulk conductance, G_B (c.f. Figure 20). As discussed in detail elsewhere [32], the components of the parallel admittance in this model are given by Eqs.12 and 13 respectively:

$$\omega C_p = \frac{\omega C_{sc} G_B^2}{G_B^2+(\omega C_{sc})^2} \tag{12}$$

$$G_p/\omega = \frac{\omega C_{sc}^2 G_B}{G_B^2+(\omega C_{sc})^2} \tag{13}$$

In the above equations, ω is the angular frequency ($2\pi f$). Note that in this simplified representation, the effect of the faradaic conductance, G_F has been ignored (vide infra). According to Eqs.12 and13, plots of ωC_p vs ω and G_p/ω vs ω will have maxima at a frequency given by $\omega_{max} = G_B/C_{sc}$ such that the functions will have the values given by Eqs.8 and 9. (See Previous Section).

Illustrative plots typifying this behavior are shown in Figure 21 for the model interface at two bias voltages, 0.6V and 1.2V respectively. The crosses represent the experimental data.

Computer programs have been developed in this laboratory to automatically determine the maximum values of the functions (given by Eqs. 8 and 9) from ωC_p vs ω and G_p/ω vs ω plots. For the particular examples shown in Figure 21, C_{sc} was calculated to be 33,300 pF and 21,400 pF at 0.6V and 1.2V respectively. In a similar fashion, G_B was calculated from ωC_p vs ω plots (not shown) to be 5.1×10^{-3} mho. The expected insensitivity of G_B to the applied bias was confirmed in these analyses. Using the above values of C_{sc} and G_B, "theoretical" G/ω vs ω plots were constructed; these are shown in Figure 21 as solid lines. The degree of fit of these lines to the data points provides an accurate measure of the accuracy in the determination of the function maxima (and therefore G_B and C_{sc} via Eqs. 8 and 9).

Using the "frequency-independent" C_{sc} values calculated from the above analyses as a function of bias voltage, a Mott-Schottky plot was constructed for the test interface as shown in Figure 23. A V_{fb} value of 0.090 ± 0.005V is estimated from this plot. The degree of reproducibility was tested by two separate experiments on the same electrode/electrolyte combination. The calculated C_{sc} values in the two cases agreed to within 2% over the entire voltage range. The corresponding V_{fb} values differed by 11 mV.

Figure 21 A (See Next Page)

Experimental (crosses) and theoretical (solid curves) G_p/ω vs ω plots for the n-GaAs/$A\ell Cl_3$-BPC interface. The electrolyte had ~2:1 ($A\ell Cl_3$:BPC) mole ratio composition. The data at two bias voltages (0.6V and 1.2V) are shown. Solid curves a and a' represent two-element models (C_{sc} at 0.6V = 33,300 pF, C_{sc} at 1.2V = 21,900 pF, $G_B = 5.1 \times 10^{-3}$ mho). Solid curves b and b' represent behavior predicted by the complete model including surface states and faradaic conductance elements at 0.6V and 1.2V respectively. In these models, C_{sc} = 33,300 pF, $G_F = 1 \times 10^{-5}$ mho, $G_{ss}^1 = 8.1 \times 10^{-5}$ mho, C_{ss}^1 = 75,500 pF, $G_{ss}^2 = 1.1 \times 10^{-4}$ mho and C_{ss}^2 = 9000 pF at 0.6V. The corresponding values at 1.2V bias are: C_{sc} = 21,900 pF, $G_F = 5 \times 10^{-5}$, $G_{ss}^1 = 5.8 \times 10^{-5}$ mho, C_{ss}^1 = 65,400 pF, $G_{ss}^2 = 7.5 \times 10^{-5}$ mho and C_{ss}^2 = 6000 pF. $G_B = 5.1 \times 10^{-3}$ mho and is independent of bias voltage.

Figure 21 B (See Next Page)

Experimental (crosses) and theoretical (solid lines) G_p/ω vs ω plots for simulated model circuits. Curves a, b and c represent behavior predicted by two-element, three-element and the complete model including surface states respectively. In these computations, C_{sc} = 32,900 pF, $G_B = 5 \times 10^{-3}$ mho, $G_F = 1 \times 10^{-5}$ mho, $G_{ss}^1 = 8.2 \times 10^{-5}$ mho, $G_{ss}^2 = 1.2 \times 10^{-4}$ mho, C_{ss}^1 = 75,900 pF and C_{ss}^2 = 9000 pF.

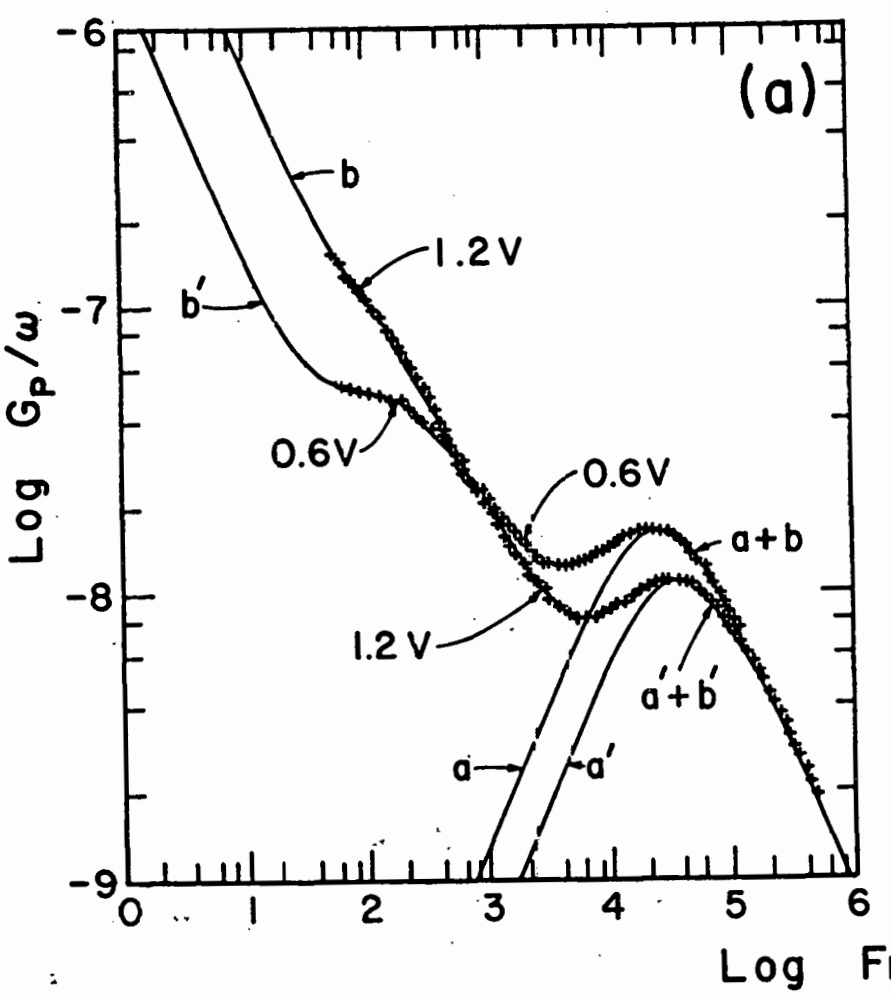

Figure 21B

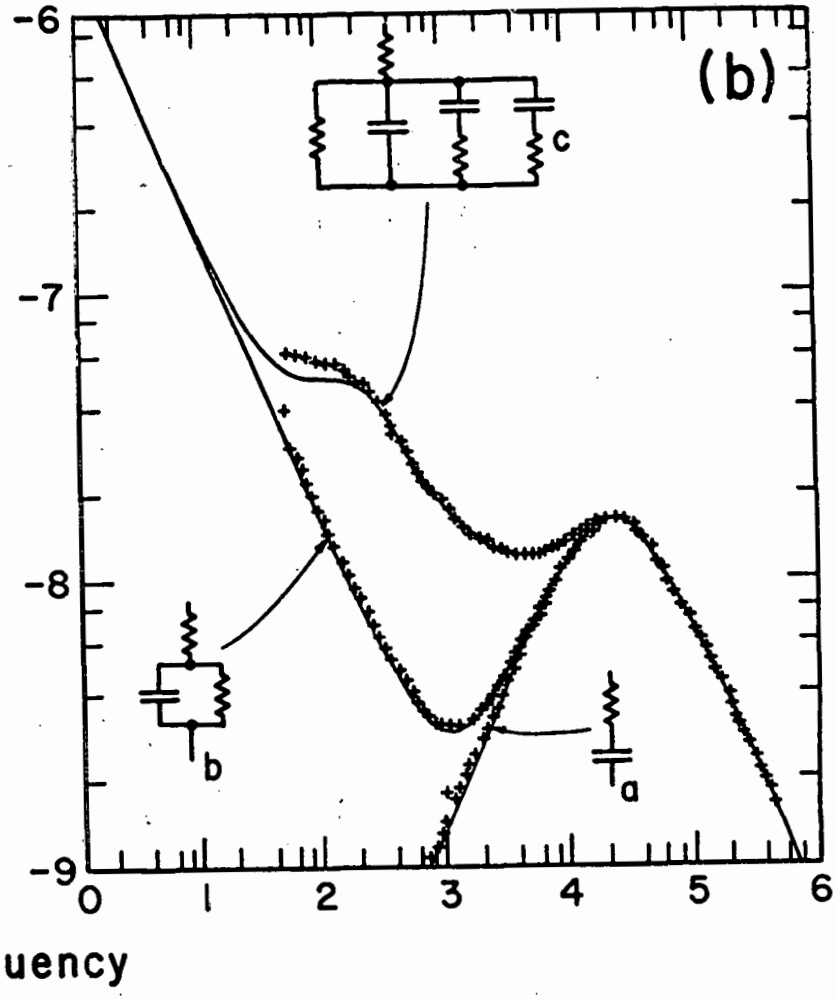

Figure 21A

An N_D value of 1.2×10^{17} cm^{-3} was deduced from the slope of the Mott-Schottky plot in Figure 22. For this calculation, ε_s was taken as 10.9 ε_o (ε_o = permittivity of free space, 8.85×10^{-14} F/cm). This calculated value could be consistent with the Hall value quoted by the manufacturer (4.5×10^{16} cm^{-3}) if a roughness factor of 1.6 is assumed for the electrode surface area. An alternative reason for the discrepancy between the present value and that quoted by the manufacturer could be as follows. Hall measurements are sensitive only to free (dissociated) charges and often the impurities are only incompletely ionized whereas in capacitance techniques, the field across the depletion layer often provides a more complete ionization of the donor atoms with a consequent increase in the measured N_D value. While the N_D values obtained from capacitance measurements were in each case significantly higher than the corresponding Hall data for n-GaAs electrodes for a wide range of doping densities (as well as for n-CdSe thin film electrodes, (see above) it is indeed likely that factors related to surface roughness also play an important role in view of the extreme sensitivity of the measured slopes to the electrode surface area. Precedence exists in the literature for discrepancies between measured slopes and those predicted from Hall data [43,44]. For example, Janietz et al. [44] report that N_D values obtained from Mott-Schottky analysis on n-GaAs and n-GaP electrodes are ~25% higher than those measured by the Hall technique.

Having established that meaningful C_{sc} values may be extracted from the simple, two-element C_{sc}-G_B model (c.f. Eqs. 12 and 13), the following question arises: What effect does the inclusion of the G_F term (c.f. Figure 20) have on the peak maximum caused by the C_{sc}-G_B

combination? Computer simulations show that unless the G_F term becomes very large, it will not overlap with the peak caused by the C_{sc}-G_B combination [38,39]. The more ideally polarized the interface, the smaller the G_F value and hence the lower the frequency range at which it will have an appreciable effect. The importance of ensuring complete polarization of the interface has been stressed by previous authors [36]. The theoretical G_p/ω vs ω curves after inclusion of the G_F term are also shown in Figure 21. Note that the G_B-C_{sc} peaks are not influenced by the addition of this extra circuit element showing that the influence of G_F is confined to lower frequencies. The relevant equations for the three-element model are detailed elsewhere [38,39] since they are not germane to the objectives of this paper.

How do surface states affect the G_B-C_{sc} peaks? Computer simulations again show that the critical factor here is the peak frequency, ω_{max}^{ss} caused by the particular surface G-C state (c.f. Figure 20). When ω_{max}^{ss} for such a state occurs between that caused by the C_{sc}-G_B combination and the low frequency G_F peak, a hump may appear in the G_p/ω vs ω plots in the intermediate frequency regime depending on the relative magnitudes of C_{sc} and the surface-state capacitance [38 39]. On the other hand if ω_{max}^{ss} located very near the peak frequency of the G_B-C_{sc} state, or at very low frequencies (near the G_F effect), its effect will be difficult to discern from the theoretical curve for the C_{sc}-G_B-G_F model (c.f. Figure 20). In this case, the surface states will primarily cause a broadening of the low-frequency shoulder in the G_B-C_{sc} peak. Interestingly enough, behavior typifying both these cases, is seen for the n-GaAs/AℓCℓ_3-BPC interface. Both a low-frequency surface state as well as a high-frequency state have been located at the

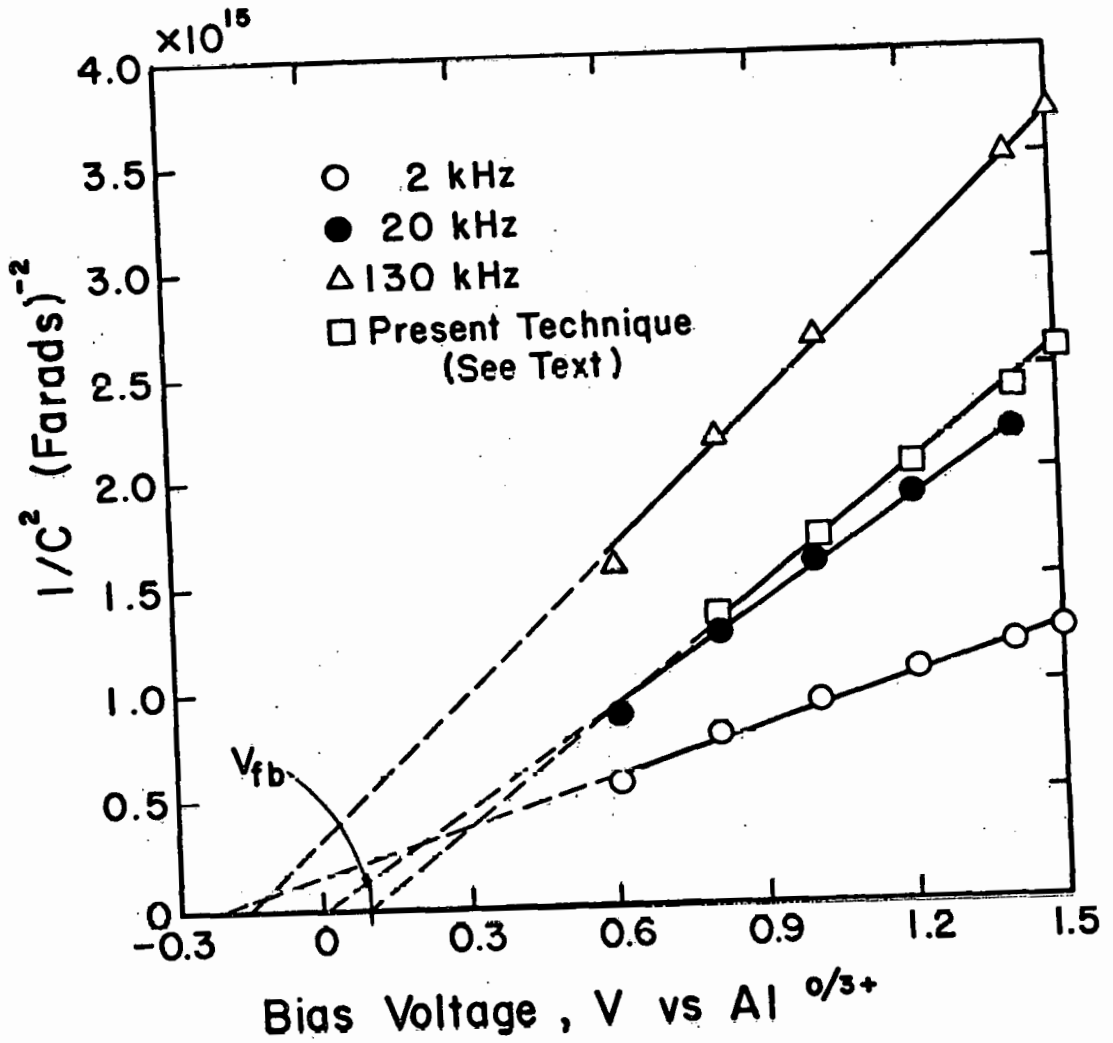

Figure 22

Mott-Schottky plots for the n-GaAs/AℓCℓ_3-BPC interface constructed from admittance data. The data using both "frequency-independent" parameters (c.f. Eq. 8, see text) as well as C_s values at discrete frequencies (2 kHz, 20 kHz and 130 kHz respectively) are compared.

n-GaAs/$A\ell C\ell_3$-BPC interface as discussed elsewhere [38]. The theoretical curves incorporating surface states are also shown in Figure 21. While procedural details for these computations are discussed elsewhere [38, 39], we note, for the purposes of the present study, that computation of C_{sc} values is not complicated even in the presence of such states.

The focal point of the above discussion is simply that, for Mott-Schottky analyses, it most often suffices to consider only the simplified two-element model, except perhaps in extreme situations where the G_B-C_{sc} peak is severely distorted by deleterious effects. We have not observed instances of such behavior either on the present interface or for other electrode/electrolyte junctions (e.g. n-CdSe/polysulfide interface, see above.

The above conclusions were confirmed by response curves obtained from simulated model circuits of varying complexity (c.f. Figure 20). Typical results are shown in Figure 21 Precision low-loss capacitors and metal film resistors were used for these measurements. The values chosen for these components typify those observed for semiconductor/electrolyte junctions. In each case shown in Figure 21, the value computed for C_{sc} (via Eq. 8) differed by less than 0.5% of the actual value, confirming the relative insensitivity of the computed C_{sc} value to the model complexity (vide supra).

The dangers inherent in the interpretation of Mott-Schottky data obtained from measurements at discrete frequencies (which are often arbitrarily chosen) are illustrated by the expermental data in Figures 22 and 23 and by the simulated models data in Figure 23. The data in Figures 22 and 23 were obtained from the same experiments as before (c.f. Figure 21 but analyzed in a different manner. For these analyses, the

Figure 23 A (See Next Page)

Experimental (crosses) and theoretical (solid curve) C_s vs ω data for the n-GaAs/$A\ell Cl_3$-BPC device at two bias voltages (0.6V and 1.2V). The theoretical curves were generated using the same parameters as in Figure 2a.

Figure 23B

Experimental (crosses) and theoretical (solid curve) C_s vs ω data for simulated model circuits. Curves a, b and c correspond to those in Figure 2b.

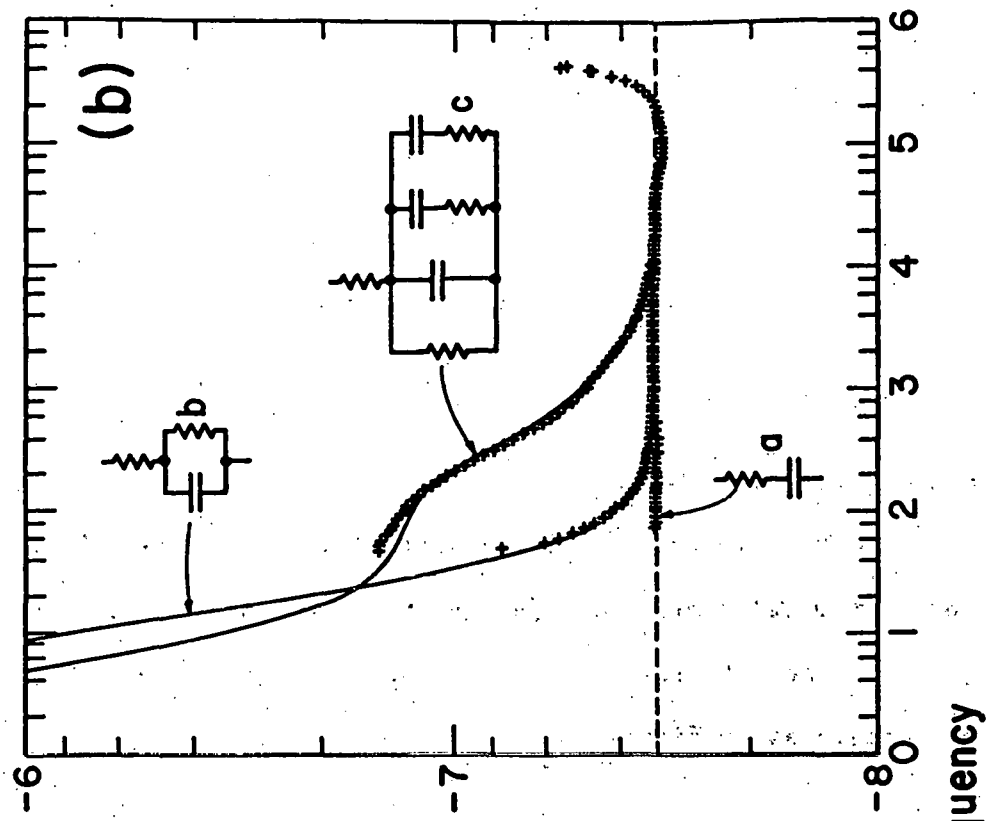

Figure 23A

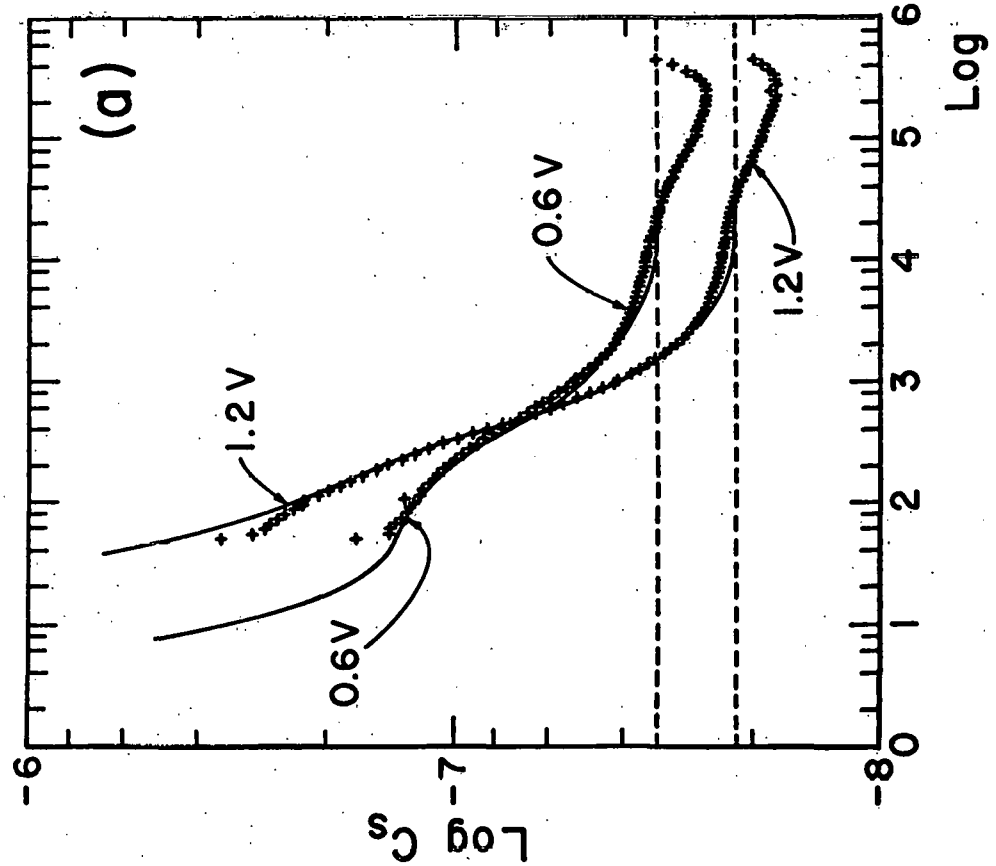

Figure 23B

parallel C_p value measured at each individual frequency was converted to its series equivalent [45]. The Mott-Schottky data for three such frequencies are shown in Figure 22. Note that the assignment of unique frequency-independent V_{fb} and N_D values now becomes ambiguous for the same system for which such values were defined by our modified analysis procedure (vide supra).

The reason why this is so becomes clear from an examination of the data in Figure 23. In Figure 23, the "frequency-independent" C_{sc} values determined by the present technique are shown as horizontal dashed lines at the two bias voltages corresponding to the data in Figure 21. The experimental data (shown as crosses in Figure 23) coincide with these values only over a very narrow frequency range. At higher frequencies, dipolar relaxation effects in the space-charge layer such as those described by previous authors [46] cause frequency dispersion whereas at lower frequencies, effects caused by faradaic processes and surface states cause large departures from "ideal" frequency-independent behavior. The subsequent increase in the C_s values at very high frequencies may be attributed to amplifier "roll-off" which places an upper limit for the frequency range accessible for measurement.

The data on the simulated model circuits in Figure 23 provide evidence which confirms the results on the semiconductor/electrolyte junction. The crosses again represent experimental data points. The solid line labelled 'a' represents the theoretical curve for the two-element circuit and curves b and c represent the behavior resulting from the successive addition of G_F and surface states to the model circuit (c.f. Figure 20). One point worthy of note in Figure 23 is the absence of the high-frequency dispersion characteristic of the

semiconductor/electrolyte junction (c.f. Figure 23). This tends to support the above interpretation of this effect in terms of dipolar relaxation effects in the semiconductor space-charge layer.

In conclusion, a new analysis procedure has been described for the determination of Mott-Schottky parameters from admittance measurements. This procedure permits unequivocal assignment of Mott-Schottky intercepts and slopes such that the interfering effects of faradaic processes, surface states and other frequency dispersion phenomena, are precluded. The dangers inherent in the interpretation of Mott-Schottky data, based on measurements at discrete or arbitrarily chosen frequencies, are illustrated by the results on a representative semiconductor/electrolyte junction as well as by data on simulated model circuits. Theoretical plots constructed from equivalent-circuit models provide further confirmation of the utility of the proposed technique.

5. PROJECTED RESEARCH

Efforts are continuing at further understanding of the n-GaAs/$AlCl_3$-BPC interface by admittance measurements. The variables for these studies are electrode doping density and electrolyte composition. Helmholtz layers effects will be of particular relevance to this program phase.

Capacitance measurements on the InP (n and p)/$AlCl_3$-BPC and n- and p- GaP/$AlCl_3$-BPC junctions are underway.

6. REFERENCES AND NOTES

1. (a) P. Singh, K. Rajeshwar, J. DuBow and R. Job, J. Am. Chem. Soc. 102, 4676 (1980); (b) P. Singh and K. Rajeshwar, J. Electrochem. Soc., in press.

2. (a) K. Rajeshwar, P. Singh and J. DuBow, Electrochim. Acta 23, 117 (1978); (b) S. Kar, K. Rajeshwar, P. Singh and J. DuBow, Sol. Energy 23, 129 (1979).

3. J. Robinson and R. A. Osteryoung, J. Am. Chem. Soc. 101, 323 (1979).

4. (a) H. L. Jones, L. G. Boxall and R. A Osteryoung, J. Electroanal. Chem. 38, 426 (1972); (b) H. L. Jones and R. A. Osteryoung, J. Electroanal. Chem. 49, 281 (1974); (c) H. L. Chum, V. R. Koch, L. L. Miller and R. A. Osteryoung, J. Am. Chem. Soc. 97, 3264 (1975).

5. V. R. Koch, L. L. Miller and R. A. Osteryoung, J. Am. Chem. Soc. 98, 5227 (1976).

6. R. S. Threlkel and J. E. Bercaw, J. Organometal. Chem. 136, 1 (1977).

7. R. S. Nicolson, Anal. Chem. 37, 1351 (1965).

8. R. S. Nicolson, Anal. Chem. 38, 1406 (1966).

9. R. J. Gale, P. Singh and R. Job., J. Organometal. Chem. 199, C 44 (1980).

10. J. Robinson, R. C. Bugle, H. L. Chum, D. Koran and R. A. Osteryoung, J. Am. Chem. Soc. 101, 3776 (1979).

11. R. J. Gale and R. A. Osteryoung, J. Electrochem. Soc. 127, 2167 (1980).

12. P. Singh, Ph.D. Thesis, Colorado State University, Fort Collins, Colorado (1980).

13. P. Singh, R. Singh, R. Gale, K. Rajeshwar and J. DuBow, J. Appl. Phys. 51, 6286 (1980).

14. H. Gerischer in "Physical Chemistry--An Advanced Treatise," Vol. 9A, H. Eyring, editor, Academic Press, New York, p. 170, Chapter 5.

15. A. J. Bard, A. B. Bocarsly, F. F. Fan, E. G. Walton and M. S. Wrighton, J. Am. Chem. Soc. 102, 3671 (1980).

16. S. R. Morrison, "The Chemical Physics of Surfaces," Chapter 8, p. 280, Plenum Press, New York (1977).

17. (a) A. B. Bocarsly, D. C. Bookbinder, R.N. Dominey, N.S. Lewis and M.S. Wrighton, J. Am. Chem. Soc. 102, 3683 (1980); (b) L.F. Schneemeyer and M.S. Wrighton, J. Am. Chem. Soc. 102, 6964 (1980); (c) A. Aruchamy and M.S. Wrighton, J. Phys. Chem. 84, 2848 (1980).

18. R. C. Kainthla, D. K. Pandya and K. L. Chopra, This Journal 127, 277 (1980).

19. I.J. Kaur, D.K. Pandya and K.L. Chopra, This Journal 127, 943 (1980).

20. G. Hoes, Nature 285, 29 (1980).

21. R. C. Kainthla, D.K. Pandya and K.L. Chopra, Appl. Phys. Lett (communicated).

22. E. H. Rhoderick, "Metal-Semiconductor Contacts," Clarendon Press, Oxford, 1978, p. 9.

23. K. T. L. DeSilva and D. Haneman, This Journal 127, 1554 (1980).

24. D. Cahen, G. Hodes and J. Manassen, This Journal 125, 1623 (1978).

25. R. N. Noufi, P. A. Kohl, J. W. Rogers Jr., J. M. White and A. J. Bard, This Journal 126, 949 (1979).

26. Ref. 22, p. 7.

27. A. B. Ellis, S. W. Kaiser, J. M. Bolts and M. S. Wrighton, J. Amer. Chem. Soc. 99, 2839 (1977).

28. M. A. Russak, J. Reichman, H. Witzke, S. K. Deb and S. N. Chen, Paper No. 240, 155th Electrochem. Soc. Meeting, Boston, MA (1979).

29. B. Miller, A. Heller, M. Robbins, S. Menezes, K. C. Chang and J. Thomson Jr., This Journal 124, 1019 (1977); A. Heller, G. P. Schwartz, R. G. Vadimsky, S. Menezes and B. Miller, This Journal 125, 1156 (1978).

30. S. N. Frank and A. J. Bard, J. Am. Chem. Soc. 97, 7427 (1975).

31. R.N. Noufi, P. A. Kohl, S.N. Frank and A.J. Bard, This Journal 125, 246 (1978).

32. P. Smith. M.S. Thesis, Colorado State University, Fort Collins, Colorado (1980), Unpublished.

33. R.N. Noufi, P.A. Kohl and A.J. Bard, This Journal 125, 375 (1978).

34. Ref. 22, p. 36.

35. A. Manabe, A. Mitsuishi and H. Yoshinaga, Jap. Journal Appl. Phys. 6, 593 (1967).

36. F. Carbon and W.P. Gomes, J. Phys. D 11, 163 (1978).

37. E.H. Nicollian and A. Goetzberger, Bell System Tech. J. 46, 1055 (1967).

38. R. Gale, P. Smith, P. Singh, K. Rajeshwar, and J. DuBow, ACS Symposium Ser. 146, Chap. 22, American Chemical Society (1981).

39. P. Smith, K. Rajeshwar, J. DuBow, R. Gale, J. Cooper and A. Nozik, to be submitted for publication.

40. M. Tomkiewicz in "Semiconductor Liquid-Junction Solar Cell", (A. Heller, editor), p. 92, The Electrochem. Soc., Princeton, New Jersy (1977).

41. M. Tomkiewicz, J. Electrochem. Soc. 126, 2220 (1979).

42. For the present analyses, it is assumed that $C_H >> C_{sc}$. (c.f Figure 20). The symbol "C_{sc}", however, is used with the recognition that Helmholtz layer effects may be still present. This possibility is evident in the shift observed for V_{fb} with the composition of the $AlCl_3$-BPC electrolyte (c.f. Ref. 1a).

43. T.O. Rouse and J.L. Weininger, J. Electrochem. Soc. 113, 184 (1966).

44. P. Janietz, R. Weiche, J. Westfahl, R. Landsberg, and R. Dehmlow, J. Electroanal. Chem 106, 23 (1980).

45. The approximation, $C_D \simeq C_s$ employed by previous authors (c.f. Ref. 46) is not valid here because of the non-trivial value of G_F in the present case.

46. E.C. Dutoit, R.L. Van Meirhaeghe, F. Cardon and W.P. Gomes, Ber. Bunsenges. Phys. Chem. 79 1206 (1975).

☆U.S. GOVERNMENT PRINTING OFFICE: 1981-740-145/2169